



Activated M,S co-doping (M = Ni, Co, Mn) inverse spinel oxides with mixed mechanisms for water oxidation

Hai-Jun Liu, Shuo Zhang, Ruo-Yao Fan, Bin Liu, Ren-Qing Lv, Yong-Ming Chai^{*}, Bin Dong^{*}

State Key Laboratory of Heavy Oil Processing, College of Chemistry and Chemical Engineering, China University of Petroleum (East China), Qingdao 266580, PR China

ARTICLE INFO

Keywords:

Water oxidation
Inverse spinel Fe₃O₄
Mixed OER mechanisms
Electronic structure
Membrane electrode assembly

ABSTRACT

Inverse spinels with characteristic structures are one of the most popular electrocatalytic materials, but typically have limited intrinsic activities for oxygen evolution reactions (OER). Here, taking the conventional inverse spinel Fe₃O₄ as an example, a series of M (M = Ni, Co, Mn) and S co-doped Fe₃O₄ OER catalysts are selected by the guidance from theoretical simulations, and then experimentally verified by hydrothermally growing M and S co-doped Fe₃O₄ on iron foams (M,S-Fe₃O₄/IF). Based on experimentally and theoretically investigating their OER performance, M,S-Fe₃O₄/IF are considered to follow mixed OER mechanisms including adsorbate evolution mechanism and lattice oxygen mechanism, and Ni,S-Fe₃O₄/IF and Co,S-Fe₃O₄/IF display low overpotentials of 276 and 300 mV at 100 mA cm⁻², respectively. Particularly, the Co atoms into S-Fe₃O₄/IF serve as promoters for in-situ Fe dissolution and redeposition of electrochemical reconstruction during alkaline OER processes. This work contributes new avenues for designing spinel-type materials with mixed OER mechanisms.

1. Introduction

Since the concept of “Carbon peak, carbon neutralization” was proposed by the international community, hydrogen (H₂) has attracted the attention of researchers because of its high energy density and zero CO₂ emission [1–3]. As one of ideal approaches to produce H₂, electrochemical water splitting can transform excess electric energy from renewable sources into H₂ (H₂O → H₂ + 1/2 O₂, including oxygen evolution reaction and hydrogen evolution reaction) [4–9]. However, the sluggish multiply electron transfer process and rigid O–O double bond for oxygen evolution reaction (OER) blocks the electrochemical overall water splitting [10–15]. From the view of the accessible and practical application of electrochemical water splitting, the development of endurance and efficient OER electrocatalysts with earth-abundant raw materials and time-saving preparation methods is particularly essential.

Among transition-metal-based OER catalysts, inverse spinel materials are inexpensive, easy to synthesise, structurally stable and have good electrical conductivity [16]. The rich elemental composition of Fe-based inverse spinel materials can provide active sites with unique electronic structures [17,18]. However, due to the lack of effective strategies that can increase the electrocatalytic active sites and modulate their intrinsic catalytic activity, the electrocatalytic activity of Fe-based

inverse spinel oxides is still to be significantly enhanced compared to other conventional electrocatalytic materials such as noble metals.

In addition, the conventional volcanic structure-activity relationship built against the surface adsorption can be used as a guideline for screening OER catalysts, however, the complexity of the OER mechanism on the Fe-based inverse spinel oxides leads to the limitation of this method. Additional opportunities to further enhance OER activities may hide in the inherent features of Fe-based inverse spinel electrocatalysts, which is influential as well in mass charge transfer within electrocatalysts and between reactants and electrocatalysts [19]. Indeed, recent studies have highlighted that electrocatalytic activities of Fe-based inverse spinel oxides can be distinctly influenced by the change of inherent features such as charge distribution, spin state, and magnetic ordering. Heterogeneous elemental doping is the most common regulation strategy to modulate the OER activity of Fe-based inverse spinel oxides, including metal and non-metal elemental doping, due to the modified electronic structure and the adsorption energy [20]. Han et al. [21] reported that metal Co doping can improve the OER catalytic activity of Fe₃O₄; Zhang et al. [22] successfully synthesized F, P double-doped Fe₃O₄ on iron foam substrate. However, the exact motivations for the improved electrocatalytic performance of Fe₃O₄ upon heterogeneous elemental doping are rather inexplicit. Moreover, OER conditions are harsh, and Fe-based inverse spinel catalysts will undergo surface

^{*} Corresponding authors.

E-mail addresses: ymchai@upc.edu.cn (Y.-M. Chai), dongbin@upc.edu.cn (B. Dong).

<https://doi.org/10.1016/j.apcatb.2023.123567>

Received 10 September 2023; Received in revised form 6 November 2023; Accepted 25 November 2023

Available online 29 November 2023

0926-3373/© 2023 Elsevier B.V. All rights reserved.

reconstruction, and conversion to Fe oxyhydroxide [17], which can serve as fresh active sites for OER. Therefore, reasonable elemental doping to achieve a rational design of the catalyst surface reconstruction with the enhanced OER activity is worthy of attention.

Based on this, the optimized crystal units of inverse spinel Fe_3O_4 were compared with those of Fe_3O_4 doped with S and first-row transition metal ($M = \text{Sc}, \text{Ti}, \text{V}, \text{Cr}, \text{Mn}, \text{Co}, \text{Ni}, \text{Cu}, \text{Zn}$) through density functional theory (DFT) calculations (Fig. 1 and S1). The MO_5 octahedrons cause the Fe atoms in the centre of the adjacent octahedron to be modulated, which is typically the OER active site of Fe-based inverse spinel oxides. The distortion level of FeO_6 octahedrons can be evaluated by the bond angle variance (BAV) [23]. The BAV values (quantifying the distortion from O-Fe-O angles inside the FeO_6 octahedron) are increased to the optimal value by Mn, Fe, Co and S co-doping, revealing that extraordinary lattice distortions can be caused (Fig. 1a).

In addition, it is clearly observed that M and S co-doping strategies can have a significant modulating effect on the electronic structure of Fe sites in Fe_3O_4 , which is well supported by the reduction of the Bader charge of Fe sites (Fig. 1a). Among them, Mn, Fe, Co and S co-doping strategies have a more obvious effect on the modulation of the Bader charge of Fe sites in Fe_3O_4 . An observable correlation between lattice distortions and Bader charge implies that the regulation of electronic structure by the M and S co-doping strategy is partly related to the Jahn-Teller effect. According to the theory of the Jahn-Teller effect, lattice distortions will further affect the electronic structure of the central Fe^{3+} , and lead to one e_g electron of Fe^{3+} in the octahedral position to flow to t_{2g} orbital with lower energy (Fig. 1b) [24]. Regulating spin configuration from high spin ($t_{2g}^3e_g^2$) to medium spin ($t_{2g}^4e_g^1$) leads to superior adsorption capacities and catalytic kinetics for OER intermediates on Fe^{3+} in the center of octahedron [25]. And actual OER activities of Mn,S- Fe_3O_4 , Co,S- Fe_3O_4 , Ni,S- Fe_3O_4 were are legitimately expected.

Therefore, a series of Fe_3O_4 nanosheets on iron foams doped with different transition metal atoms ($M = \text{Ni}, \text{Co}, \text{Mn}$) and S atoms have been

selected to synthesize via a simple and easy to scale-up hydrothermal method (Fig. 2a). The foreign atoms are in situ doped into the Fe_3O_4 lattice, which significantly results in lattice distortions of FeO_6 octahedrons, alters the electronic structure of Fe_3O_4 , and thus affects the electrocatalytic OER performance of Fe_3O_4 . The obtained Ni,S- Fe_3O_4 /IF exhibits the best OER electrocatalytic performance (276 mV vs. RHE at 100 mA cm^{-2} , 312 mV vs. RHE at 500 mA cm^{-2} in 1.0 M KOH) among all the catalyst investigated, and remains stable during long-term stability tests at industrial-level current densities. Among M,S- Fe_3O_4 /IF catalysts, only Co,S- Fe_3O_4 /IF has been found to undergo an operando reconstruction process to form active Fe oxyhydroxides in alkaline condition during OER. Moreover, taking advantage of theoretical calculations, it reveals that M and S co-doping strategies can change rate-determining steps (RDS) and reduce RDS barriers in the OER processes following both the adsorbate evolution mechanism (AEM) and the lattice oxygen mechanism (LOM). To better match theoretical OER performance with experimental OER performance, a mixed OER mechanism including both AEM and LOM is innovatively proposed. The AEM mechanism ensures the stability of the crystal structure, and the LOM mechanism can break the scaling relationship between ΔG_{OOH} and ΔG_{OH} , the mixing mechanism provides more possibilities for improving the performance of OER catalysts. Furthermore, the relationship between the 3d orbital of the transition metal and the 2p orbital of O can be considered as an important indicator to assess the proportion of the LOM mechanism. This work offers a reasonable elemental doping reference to achieve OER catalyst designs, taking full account of electronic effects, lattice distortions, and surface reconstruction behaviours in practical electrochemical tests.

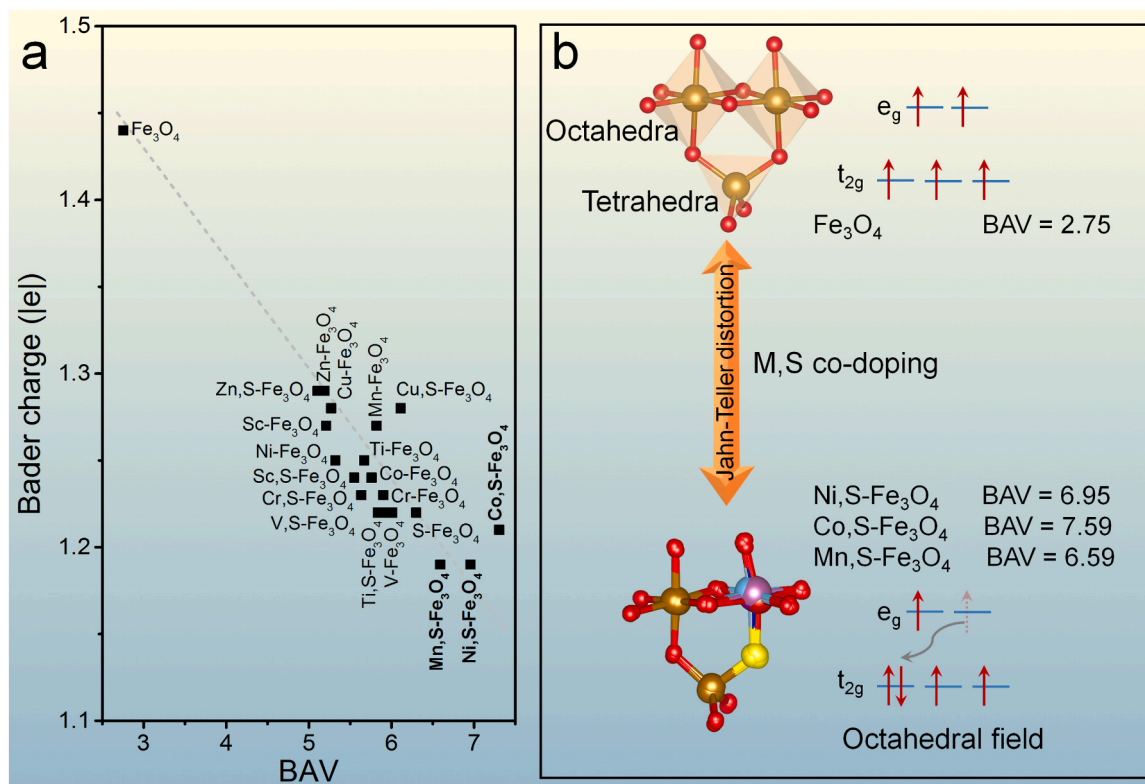


Fig. 1. a) Relationship between bond angle variance (BAV) and bader charge of Fe atoms for Fe_3O_4 , M- Fe_3O_4 , and M,S- Fe_3O_4 ($M = \text{first-row transition metal: Sc, Ti, V, Cr, Mn, Co, Ni, Cu, Zn}$). b) The orbital splitting of Fe^{3+} 3d in Fe_3O_4 and M,S- Fe_3O_4 under octahedral geometry. Brown ball: iron atom; blue ball: Ni, Co, Mn atom; yellow ball: sulfur atom; red ball: oxygen atom.

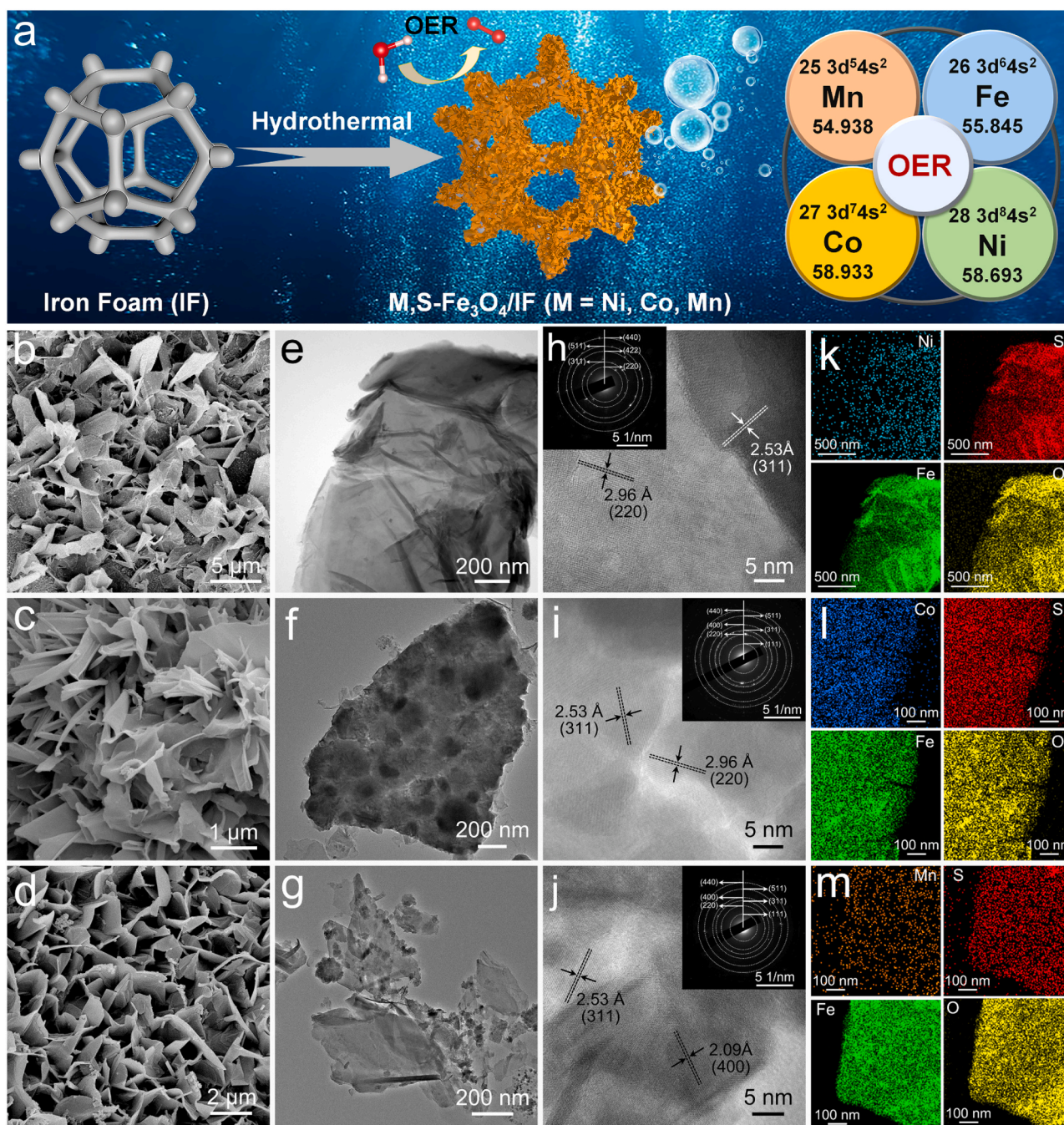


Fig. 2. a) Schematic illustration of the formation process of M,S-Fe₃O₄/IF (M = Ni, Co, Mn). SEM images of b) Ni,S-Fe₃O₄/IF, c) Co,S-Fe₃O₄/IF and d) Mn,S-Fe₃O₄/IF. TEM images of e) Ni,S-Fe₃O₄/IF, f) Co,S-Fe₃O₄/IF and g) Mn,S-Fe₃O₄/IF. HRTEM images and corresponding SAED patterns of h) Ni,S-Fe₃O₄/IF, i) Co,S-Fe₃O₄/IF and j) Mn,S-Fe₃O₄/IF. HAADF-STEM-EDS mapping of k) Ni,S-Fe₃O₄/IF, l) Co,S-Fe₃O₄/IF and m) Mn,S-Fe₃O₄/IF.

2. Experimental section

2.1. Syntheses of Ni,S-Fe₃O₄/IF, Co,S-Fe₃O₄/IF, Mn,S-Fe₃O₄/IF

Ni,S-Fe₃O₄/IF, Co,S-Fe₃O₄/IF and Mn,S-Fe₃O₄/IF was prepared via the hydrothermal method. In a typical synthesis of Ni,S-Fe₃O₄/IF, 0.2 mmol NiSO₄·6 H₂O and 24 mmol CH₄N₂S were dissolved in 60 mL deionized water and stirred continuously at room temperature for 10 min to form a uniform solution. Then, the solution containing a piece of Fe foam (2.0 cm × 5.0 cm) hydrothermally treated at 140 °C for 4 h. In this process, IF is both a substrate and an iron source; NiSO₄·6 H₂O is the Ni source; and the CH₄N₂S serves as the S source. After 4 h, the color of the IF was changed from its original metal luster to black. The

preparation process of Co,S-Fe₃O₄/IF and Mn,S-Fe₃O₄/IF was similar to that of Ni,S-Fe₃O₄/IF, except that replacing CoCl₂·6 H₂O with CoSO₄·7 H₂O and MnSO₄·H₂O in the hydrothermal treatment process, respectively.

2.2. Syntheses of Ni-Fe₃O₄/IF, Co-Fe₃O₄/IF, Mn-Fe₃O₄/IF

For comparison, Ni-Fe₃O₄/IF, Co-Fe₃O₄/IF, and Mn-Fe₃O₄/IF were also synthesized by hydrothermal method. The preparation process of Ni-Fe₃O₄/IF, Co-Fe₃O₄/IF, Mn-Fe₃O₄/IF was similar to that of Ni,S-Fe₃O₄/IF, Co,S-Fe₃O₄/IF, Mn,S-Fe₃O₄/IF, except that NiSO₄·6 H₂O, CoCl₂·6 H₂O and MnSO₄·H₂O was removed in the hydrothermal treatment process, respectively.

2.3. Syntheses of S-Fe₃O₄/IF and Fe₃O₄/IF

For comparison, S-Fe₃O₄/IF and Fe₃O₄/IF were also prepared via hydrothermal method. The synthesis process of S-Fe₃O₄/IF is similar to that of Ni,S-Fe₃O₄/IF, except for the remove of NiSO₄·6 H₂O in the hydrothermal treatment. The synthesis process of Fe₃O₄/IF is similar to that of S-Fe₃O₄/IF, except for the remove of CH₄N₂S in the hydrothermal treatment.

3. Results and discussion

3.1. Characterization of morphology and structure of M,S-Fe₃O₄/IF (M = Ni, Co, Mn)

The crystal phases of M,S-Fe₃O₄/IF were first investigated by the X-ray powder diffraction (XRD). From XRD results, the diffraction peaks of

all samples can be indexed to the inverse spinel structure of the Fe₃O₄ (JCPDS Card No. 01-089-3854) with no collateral peaks (Fig. S2a). It is worth noting that, compared with M-Fe₃O₄/IF and Fe₃O₄/IF, the inverse spinel structure remains basically unchanged after the S incorporation, while the peaks are shifted slightly to high angles, further confirming the formation of M and S co-doped Fe₃O₄ crystals on IF (Fig. S2b). The morphology of the catalysts was investigated by scanning electron microscopy (SEM) and transition electron microscopy (TEM). As shown in Fig. S3, pure IF has a 3D porous skeleton structure and smooth surface. The Ni,S-Fe₃O₄/IF (Fig. 2b, S4), Co,S-Fe₃O₄/IF (Fig. 2c, S5), and Mn,S-Fe₃O₄/IF (Fig. 2d, S6) all display a special nanosheets arrays morphology, which will provide a large surface area and exposes a great number of electroactive sites for OER [26]. It can be seen that Ni, S-Fe₃O₄, Co,S-Fe₃O₄, and Mn,S-Fe₃O₄ nanosheets with a lateral size of several nanometers are homogenously grown on IF, as shown in Figs. 2b, 2c, and 2d. The low-magnification TEM images (Fig. 2e-g) further

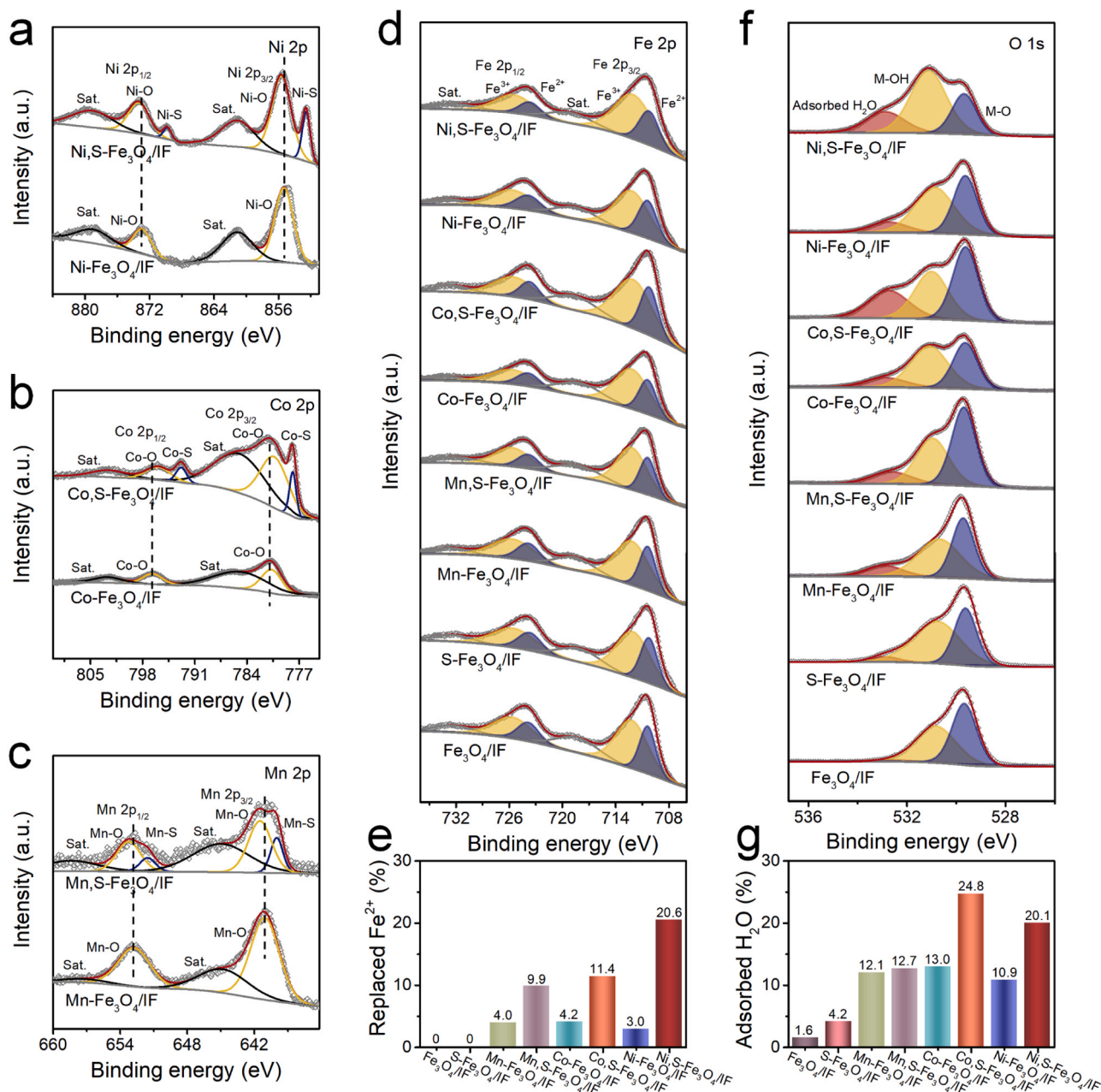


Fig. 3. a) Ni 2p, b) Co 2p, c) Mn 2p, d) Fe 2p and f) O 1s XPS spectra of Ni,S-Fe₃O₄/IF, Ni-Fe₃O₄/IF, Co,S-Fe₃O₄/IF, Co-Fe₃O₄/IF, Mn,S-Fe₃O₄/IF, Mn-Fe₃O₄/IF, S-Fe₃O₄/IF, and Fe₃O₄/IF. e) The replaced Fe²⁺ and g) the adsorbed H₂O of various samples.

confirm the nanosheet structures of M,S-Fe₃O₄, in good agreement with the observation from the SEM images. The HRTEM images in Fig. 2h-j clearly show the crystal planes with interlayer spaces of 2.53 Å, 2.96 Å and 2.09 Å corresponding to the (311), (220) and (400) lattices of the inverse spinel Fe₃O₄, respectively. The (220), (440), (311), and (511) planes detected by the selected area electron diffraction (SAED) (insert of the Fig. 2h-j) further demonstrate the successful formation of inverse spinel Fe₃O₄ phases on the IF. Moreover, the high angle annular dark-field scanning TEM (HAADF-STEM) and corresponding energy dispersive spectroscopy (EDS) elemental mapping show that Fe, O, S, and M are homogeneously dispersed in the M,S-Fe₃O₄ (Fig. 2k-m). For comparison, the M-Fe₃O₄, S-Fe₃O₄, Fe₃O₄ samples were also successfully prepared by similar hydrothermal methods, respectively (Fig. S7-S14).

In order to clarify the intrinsic electronic structure and surface chemical composition of the as-prepared M,S-Fe₃O₄/IF, S-Fe₃O₄/IF, and Fe₃O₄/IF samples, X-ray photoelectron spectroscopy (XPS) analysis was performed. As shown in the XPS survey spectra of Fig. S15, for all samples, the peaks located at 530, 284, and 710–725 eV are ascribed to O 1s, C 1s, and Fe 2p, respectively [27–29]. In the Ni 2p, Co 2p, Mn 2p, and Fe 2p spectra of samples (Figs. 3a–3d), two spin-orbit peaks, including 2p_{3/2} and 2p_{1/2}, coupled with two shake-up satellites (denoted Sat.) can be observed. In the Ni 2p spectrum of Ni,S-Fe₃O₄/IF, the peaks at 855.6 and 873.3 eV correspond to Ni 2p_{3/2} and Ni 2p_{1/2} of Ni²⁺ bonded to O (Ni-O bond), respectively [30]. In addition, compared with the Ni 2p spectrum of Ni-Fe₃O₄/IF, a new pair of peaks appears at 852.5 and 869.8 eV in the Ni 2p spectrum of Ni,S-Fe₃O₄/IF, attributed to Ni 2p_{3/2} and Ni 2p_{1/2} of the Ni-S bond. It can be noted that, compared with the Ni 2p spectrum of Ni-Fe₃O₄/IF, the Ni 2p binding energy for Ni-O in Ni,S-Fe₃O₄/IF is positively shifted by 0.4 eV, suggesting that the S incorporation leads to the enhanced coupling of the Ni-O bond. The high resolution Co 2p spectrum (Fig. 3b) of Co-Fe₃O₄/IF indicates four peaks at 802.4, 785.0, 795.9, and 780.3 eV, ascribed to the Co 2p_{3/2} and Co 2p_{1/2} of Sat. peaks and Co-O bonds, respectively [31], while two new peaks at 792.8 and 777.8 eV owing to Co-S bonds appears for Co,S-Fe₃O₄/IF. Compared with Co-Fe₃O₄/IF, the Co 2p binding energy for Co-O in Co,S-Fe₃O₄/IF exhibits a negatively shift of 0.36 eV after S-doping, revealing that the S incorporation causes the weakened coupling of Co-O bonds. Mn 2p XPS spectra (Fig. 3c) confirm the presence of Mn-O (641.5 and 653.2 eV) and Mn-S (640.0 and 651.5 eV) in the Mn,S-Fe₃O₄/IF. Compared with Mn-Fe₃O₄/IF, the Mn 2p binding energy for Mn-O in Mn,S-Fe₃O₄/IF shift to high binding energies due to the S incorporation, indicating that the S incorporation causes the enhanced coupling of Mn-O bonds. The S 2p XPS peak can be fitted into three peaks (Fig. S16). For Ni,S-Fe₃O₄/IF, for example, two peaks at 161.4 and 162.6 eV corresponded to S 2p_{3/2} and 2p_{1/2} orbitals of divalent sulfide (S²⁻), respectively [32,33]. The peak centered at 167.7 eV relates to sulfur species bonded to oxygen atoms of Fe₃O₄. In particular, a linear correlation can be found between the content of M and S doped into Fe₃O₄ lattice (Fig. S17). The effects of S doping on the electronic structure of M sites are different, resulting in enhanced Ni-O and Mn-O bonds and weakened Co-O bonds, which will allow Co,S-Fe₃O₄/IF to exhibit a different electrochemical behavior from Ni,S-Fe₃O₄/IF and Mn,S-Fe₃O₄/IF in the subsequent electrocatalytic OER processes. To better investigate the content of S element in the Ni,S-Fe₃O₄/IF, Co,S-Fe₃O₄/IF and Mn,S-Fe₃O₄/IF, the Inductively Coupled Plasma Optical Emission Spectrometer (ICP-OES) test were performed. According to the ICP-OES measurement, the mass fraction of S content in the Ni,S-Fe₃O₄/IF, Co,S-Fe₃O₄/IF and Mn,S-Fe₃O₄/IF is 1.52%, 1.16%, 0.27%, respectively.

The Fe 2p spectra can finely fitted with two spin-orbit doublets arising from 2p_{3/2} and 2p_{1/2} signals of Fe²⁺ and Fe³⁺ (Fig. 3d). By comparing the Fe 2p spectra of M,S-Fe₃O₄/IF, S-Fe₃O₄/IF, and Fe₃O₄/IF, no obvious peak movement can be observed. The doublet at 712.6 and 726.0 eV can be ascribe to Fe 2p_{3/2} and Fe 2p_{1/2} of Fe³⁺, and the doublet at 710.3 and 723.8 eV correspond to the Fe 2p_{3/2} and Fe 2p_{1/2} of Fe²⁺,

associated with their Sat. peaks centered at 718.8 and 733.0 eV [34]. In addition, due to the overlap of the Co and Ni Auger peaks with the Fe 2p peaks, conventional peak fitting method is not able to distinguish them [35]. Here, the Fe 2p_{1/2}, Ni 2p_{3/2} and Co 2p_{1/2} were used for semi-quantification of elements. Based on the Fe 2p spectra, the proportion of the substituted Fe²⁺ by Ni²⁺, Co²⁺, Mn²⁺ were calculate, and the replaced Fe²⁺ contents among the M,S-Fe₃O₄/IF, S-Fe₃O₄/IF, Fe₃O₄/IF catalyst were compared (Fig. 3e). It can be clearly seen that Fe²⁺ is most replaced by Ni²⁺ in the Ni,S-Fe₃O₄ catalyst, and the amount of Fe²⁺ substituted in the M,S-Fe₃O₄/IF sample is higher than that in the corresponding M-Fe₃O₄/IF sample. For O 1s spectra of M,S-Fe₃O₄/IF, S-Fe₃O₄/IF, Fe₃O₄/IF (Fig. 3f) both can be divided into three peaks: lattice oxygen (M-O), oxygen in hydroxyl group (M-OH), and adsorbed H₂O, respectively [18,36]. Compared with the Ni-Fe₃O₄/IF, the ratio of M-OH bond in the O 1s spectrum of Ni,S-Fe₃O₄/IF is greatly increased, and larger chemisorbed H₂O signal appears, indicating the improved adsorption capacity of Ni,S-Fe₃O₄/IF for oxygen-containing intermediates. Based on this, the adsorbed H₂O contents are compared among the M,S-Fe₃O₄/IF, S-Fe₃O₄/IF, Fe₃O₄/IF samples (Fig. 3g). The M,S-Fe₃O₄/IF and M-Fe₃O₄/IF samples have more adsorbed H₂O than the Fe₃O₄/IF sample, and the M,S-Fe₃O₄/IF and S-Fe₃O₄/IF samples have more adsorbed H₂O than the corresponding M-Fe₃O₄/IF and Fe₃O₄/IF samples without S doping, implying a synergistic effect of the co-doping strategy on the behaviour of H₂O adsorbed on the surface of Fe₃O₄-based catalysts. The high adsorbed H₂O indicates the excellent adsorption capacity of samples and ensures the kinetic rate of reactant participation at the solid-liquid-gas interface in the electrocatalytic OER process.

To better demonstrate the effect of M and S co-doping strategies on the surface properties of Fe₃O₄-based electrocatalysts, the surface wettability was then investigated by measuring the contact angle between electrolyte and electrocatalysts [37]. Fig. S18 shows that the contact angle of electrolyte on S-Fe₃O₄/IF is 132°, indicating the poor water adhesion property of S-Fe₃O₄/IF. In contrast, the liquid droplet rapidly infiltrates into the M,S-Fe₃O₄/IF samples with no contact angle observed (Fig. 4a). This reveals that M (M = Ni, Co, Mn) and S co-doped strategy delivers a super-hydrophilic surface, which is beneficial for the mass transfer between electrolyte and the surface of Fe₃O₄-based electrocatalysts in the electrocatalytic OER process [2]. In addition, Fourier transform infrared (FT-IR) spectra of different catalysts were collected to identify the surface functional groups and coordination molecules (Fig. 4b) [38]. The fingerprint peaks in the range of 500–600 cm⁻¹ assigned to the stretching vibrations of the M-O are observed for all the M,S-Fe₃O₄/IF samples [39]. For Mn,S-Fe₃O₄/IF, the fingerprint peak is observed at 572.6 cm⁻¹, and this stretching vibrational peak gets drifted to a higher value of the vibrational frequency as the Mn ions are replaced with Co and Ni ions, which can be found at around 578.3 and 585.0 cm⁻¹, respectively (Fig. 4b). This shifting in the vibrational frequency can be associated with the Hooke's law, according to which the vibrational frequency is directly proportional to the force constant and inversely proportional to the atomic mass [40]. Under the consideration of atomic masses only, the stretching vibrations of the M-O bonds should increase gradually in the order of Co-O, Ni-O, and Mn-O bonds, which is not consistent with the actual FT-IR results. Therefore, it can be inferred that the force constant of Ni-O bonds in Ni,S-Fe₃O₄/IF and Co-O bonds in Co,S-Fe₃O₄/IF is larger than Mn-O bonds in Mn,S-Fe₃O₄/IF. In other words, in M,S-Fe₃O₄/IF, the lengths of Ni-O and Co-O bonds are shorter than that of Mn-O bonds. This also well implies that the doping strategies using different transition metal elements has different effects on the lattice structure of Fe-based spinel oxides. The magnetic changes of Fe₃O₄-based samples before and after doping were investigated by vibrating sample magnetometer (VSM). The magnetic properties of Fe₃O₄-based samples are mainly provided by d electrons (Fe: 3d⁶ 4s²), but the transition metal ions are separated by larger oxygen ions with a large spacing, so there is almost no overlap part of the electron cloud between two adjacent magnetic ions and no direct Coulomb interaction.

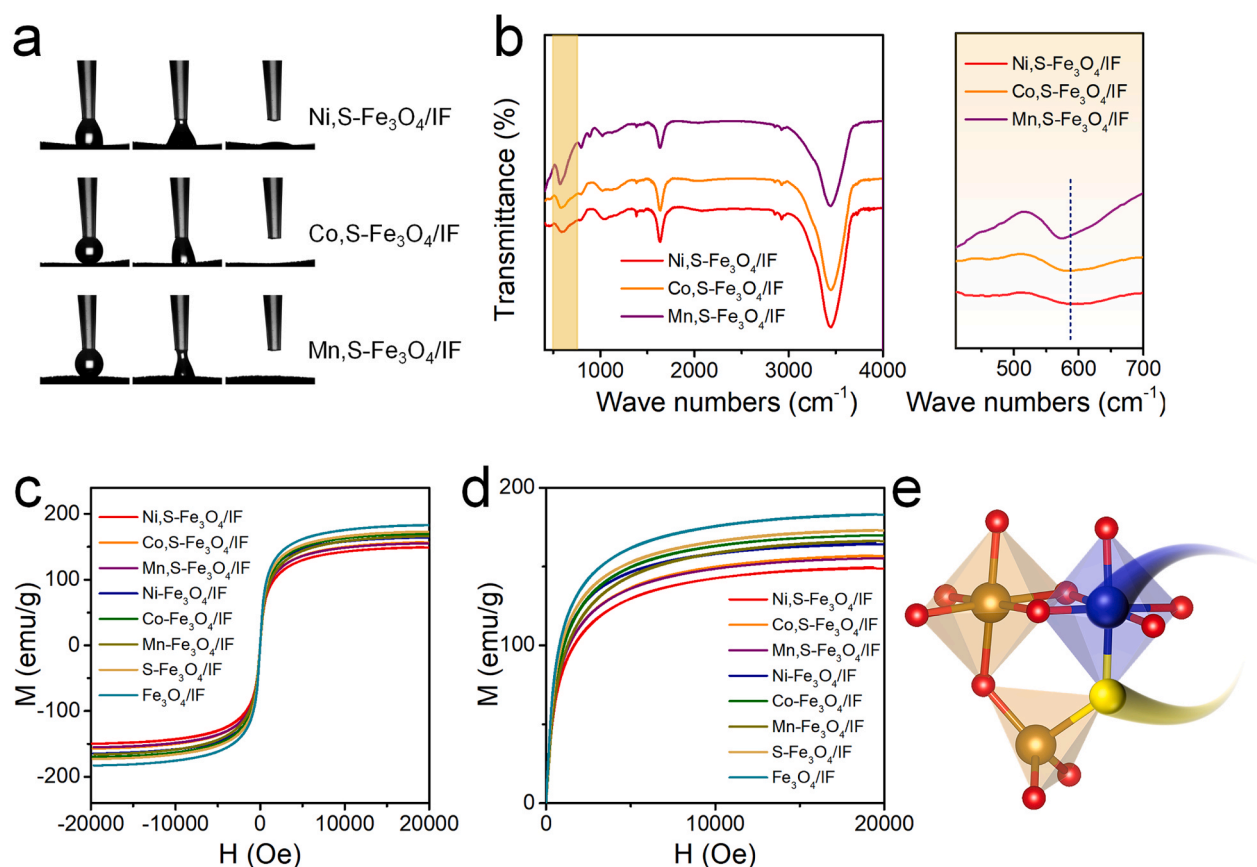


Fig. 4. a) Contact angle images of Ni,S-Fe₃O₄/IF, Co,S-Fe₃O₄/IF and Mn,S-Fe₃O₄/IF at different contact times. b) FT-IR spectra of M,S-Fe₃O₄/IF. c,d) Magnetization hysteresis loops of M, S-Fe₃O₄/IF, S-Fe₃O₄/IF, and Fe₃O₄/IF. e) The optimization model of M,S-Fe₃O₄. (Brown ball: Fe; red ball: O; yellow ball: S; blue ball: Ni, Co, Mn).

However, exchange interactions can occur between adjacent transition metal magnetic ions and intermediate oxygen ions, resulting in electron delocalisation and indirect exchange interactions, also known as superexchange interactions. The superexchange tends to make the spins antiparallel, so the inverse magnetic moments of Fe²⁺ and Fe³⁺ located on the adjacent octahedron do not cancel out and thus exhibit subferromagnetism. The ion doping causes the overlapping of the magnetic moments to be altered, as the magnetic moments of the doped ions are different from those of Fe and the resulting bond angles between the adjacent transition metal ions and O are modified [41]. The values of specific magnetization (*M_s*) are found to be reduced from Fe₃O₄/IF to M, S-Fe₃O₄/IF (Fig. 4c-d). This implies the successful co-doping of both M and S ions, and illustrates well that the doped M ions are located in the center of the octahedron originally occupied by Fe ions (Fig. 4e).

3.2. Oxygen evolution reaction performance of M,S-Fe₃O₄/IF (M = Ni, Co, Mn)

The electrocatalytic activities of as-prepared electrocatalysts for OER were first evaluated by linear scan voltammetry (LSV) using a typical three-electrode system in 1.0 M KOH aqueous electrolyte. As shown in Fig. 5a, the Ni,S-Fe₃O₄/IF sample possesses the highest OER catalytic activity among different M,S-Fe₃O₄/IF, M-Fe₃O₄/IF, S-Fe₃O₄/IF, Fe₃O₄/IF and IrO₂/IF. The overpotential of Ni,S-Fe₃O₄/IF decreases to 276 mV at 100 mA cm⁻², 92 mV lower than Ni-Fe₃O₄/IF, and 96 mV lower than S-Fe₃O₄/IF, which indicates the Ni,S co-doped strategy is responsible for the enhanced OER activity. The nanostructured Ni,S-Fe₃O₄/IF sample can steadily display high current densities of 500 and 1000 mA cm⁻² at low overpotentials of 312 and 332 mV, respectively, without

appreciable interference by intensively evolved O₂ bubbles, which meets the requirements of the industrial water splitting. In addition, it can be seen that bare IF shows a very poor OER activity, indicating the contribution of IF substrates to OER currents can be negligible. The Co,S-Fe₃O₄/IF activity is much better than S-Fe₃O₄/IF and Co-Fe₃O₄/IF, but still slightly lower than that for Ni,S-Fe₃O₄/IF. However, Mn and S co-doping has little effect on the performance improvement. The overpotential at the current density of 100 and 300 mA cm⁻² for all as-prepared samples are compared in Fig. 5b. It can be clearly seen that Ni,S-Fe₃O₄/IF delivers current densities of 100 mA cm⁻² (η_{100} = 267 mV) and 300 mA cm⁻² (η_{300} = 300 mV) outperforming those of the Co,S-Fe₃O₄/IF (η_{100} = 300 mV and η_{300} = 330 mV), Mn,S-Fe₃O₄/IF (η_{100} = 383 mV and η_{300} = 430 mV), Ni-Fe₃O₄/IF (η_{100} = 367 mV and η_{300} = 408 mV), Co-Fe₃O₄/IF (η_{100} = 347 mV and η_{300} = 373 mV), and Mn-Fe₃O₄/IF (η_{100} = 448 mV and η_{300} = 497 mV). These results demonstrate that the double doping strategies for Fe₃O₄ is very effective to improve the OER activity of Fe₃O₄, especially at larger current output, which is appreciably better than reported non-noble-metal-oxide-based OER electrocatalysts (Fig. 5c, Table S1). To exclude geometric effects [42,43], the currents are normalized by mass and Brunauer-Emmett-Teller (BET) surface areas (Fig. S19). Impressively, the Ni,S-Fe₃O₄/IF delivers a higher mass current density and a higher area current density at the same overpotential (Fig. 5d,e). Meanwhile, as demonstrated in Fig. 5f, boosted OER kinetics can be inferred by the smaller Tafel slope. The Ni,S-Fe₃O₄/IF demonstrates an extremely small Tafel slope of 45.6 mV dec⁻¹, much lower than those of Co,S-Fe₃O₄/IF (54.0 mV dec⁻¹), Mn,S-Fe₃O₄/IF (93.5 mV dec⁻¹), Ni-Fe₃O₄/IF (64.2 mV dec⁻¹), Co-Fe₃O₄/IF (58.8 mV dec⁻¹), and Mn-Fe₃O₄/IF (95.4 mV dec⁻¹). Thus, the smaller Tafel slope of Ni,S-Fe₃O₄/IF indicates more favorable

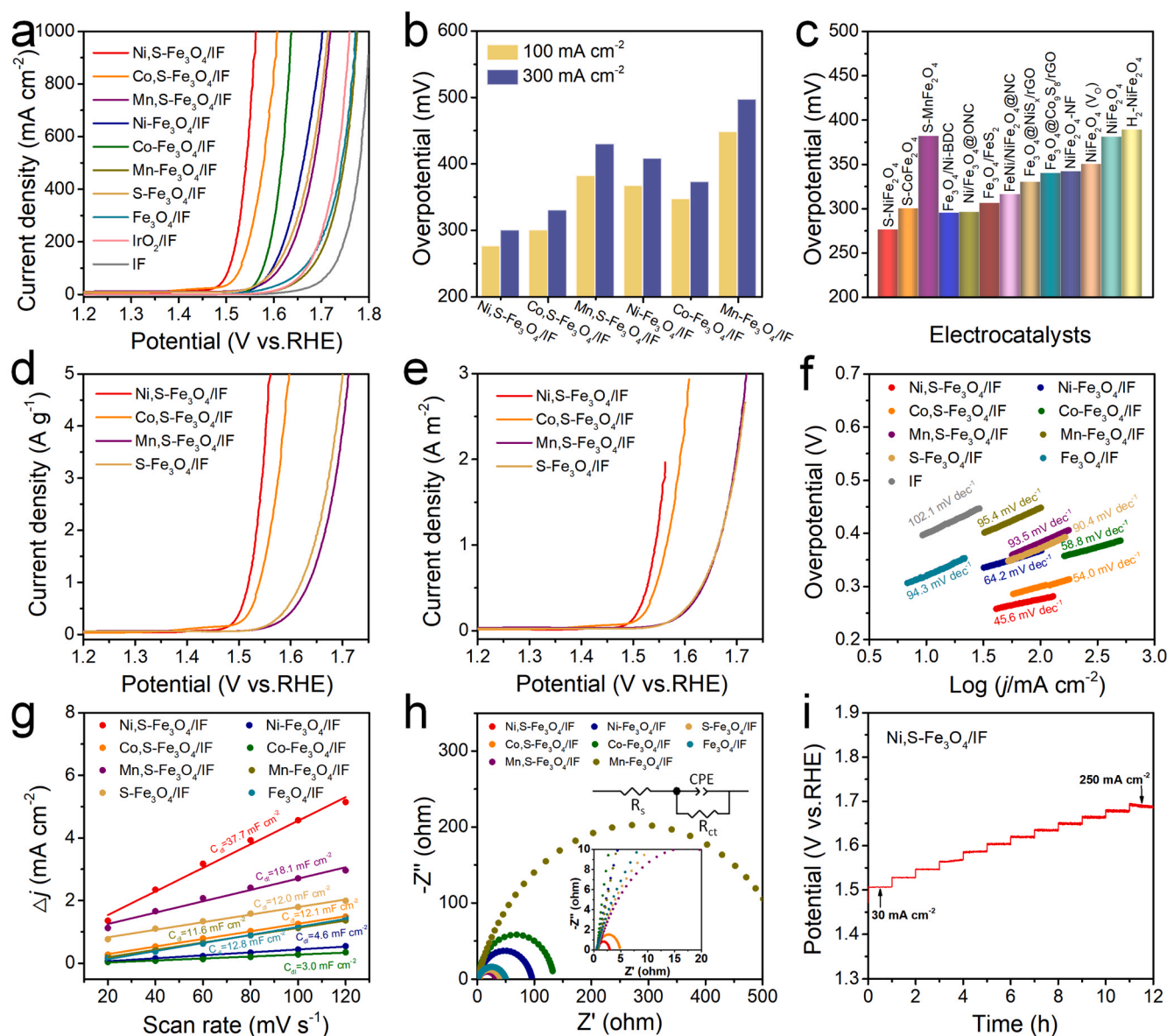


Fig. 5. a) LSV curves for OER of various samples. b) Comparison for overpotentials of various samples. c) Comparison of overpotentials for OER among samples with previously reported catalysts (Table S1). Polarization curves current normalized by d) mass and e) BET surface area of the samples. f) Corresponding Tafel plots. g) C_{dl} calculations. h) Nyquist plots of various catalysts (inset: equivalent circuit model). i) Multi-step chronopotentiometric curve of Ni,S-Fe₃O₄/IF.

reaction kinetics in the OER process [44].

The Ni,S-Fe₃O₄/IF is also superior in electrocatalytically active surface area (ECSA), as investigated by double-layer capacitances (C_{dl}) obtaining from CV measurements (Fig. 5g; Fig. S20). The C_{dl} of Ni,S-Fe₃O₄/IF is 37.7 mF cm⁻² is almost eight times larger than that of the Ni-Fe₃O₄/IF (4.6 mF cm⁻²), and three times larger than that of the S-Fe₃O₄/IF (12.0 mF cm⁻²), indicating that highly rich surface active sites are formed by a Ni and S co-doping strategy. The Ni and S co-doping Fe₃O₄ nanosheets supply accessible surface active sites, benefitting mass and charge transfer during OER processes. ECSA-normalized LSV curves indicate that Ni,S-Fe₃O₄/IF and Co,S-Fe₃O₄/IF require lower initial overpotentials to drive OER reactions, further indicating Ni,S-Fe₃O₄/IF and Co,S-Fe₃O₄/IF possess superior intrinsic OER catalytic activities (Fig. S21). In addition, electrochemical impedance spectroscopy (EIS) tests was implemented to analyse the electron transfer kinetics during OER processes. A simplified circuit model composed of electrolyte resistance (R_s), a constant phase element (CPE) and charge transfer resistance (R_{ct}) was fitted to Nyquist plots of as-prepared samples. All as-

prepared samples exhibit similar solution resistance (R_s) of about 0.8 Ω (Fig. 5h), but a significantly distinct charge transfer resistances (R_{ct}). Among all samples, the Ni,S-Fe₃O₄/IF electrode shows the smallest R_{ct} value of about 2.7 Ω , indicating the fastest electron transfer kinetics of OER is displayed on Ni,S-Fe₃O₄/IF. The multi-current step chronopotentiometric response of Ni,S-Fe₃O₄/IF was tested to show the shortened diffusion paths for OH⁻ charge carriers and fast gas bubble dissipation (Fig. 5i and S22) [45]. The rapid and retrievable potential responses from low to high current densities suggest the preminent mechanical robustness, electrical conductivity, and mass transport in the OER process on the surface of Ni,S-Fe₃O₄/IF.

The long-term stability of the Ni,S-Fe₃O₄/IF catalyst under operation for 50 h at 100 mA cm⁻², as shown in Fig. 6a. Under extended stability tests, Ni,S-Fe₃O₄/IF, Co,S-Fe₃O₄/IF, and Mn,S-Fe₃O₄/IF catalysts shows no sign of degradation after 50 h. And even, the overpotential of the Co,S-Fe₃O₄/IF sample is reduced by 18 mV at 100 mA cm⁻² during the long stability test, which can be clearly revealed by the comparison of the LSV curves before and after the 50 h stability tests (Fig. 6b-d). o further study

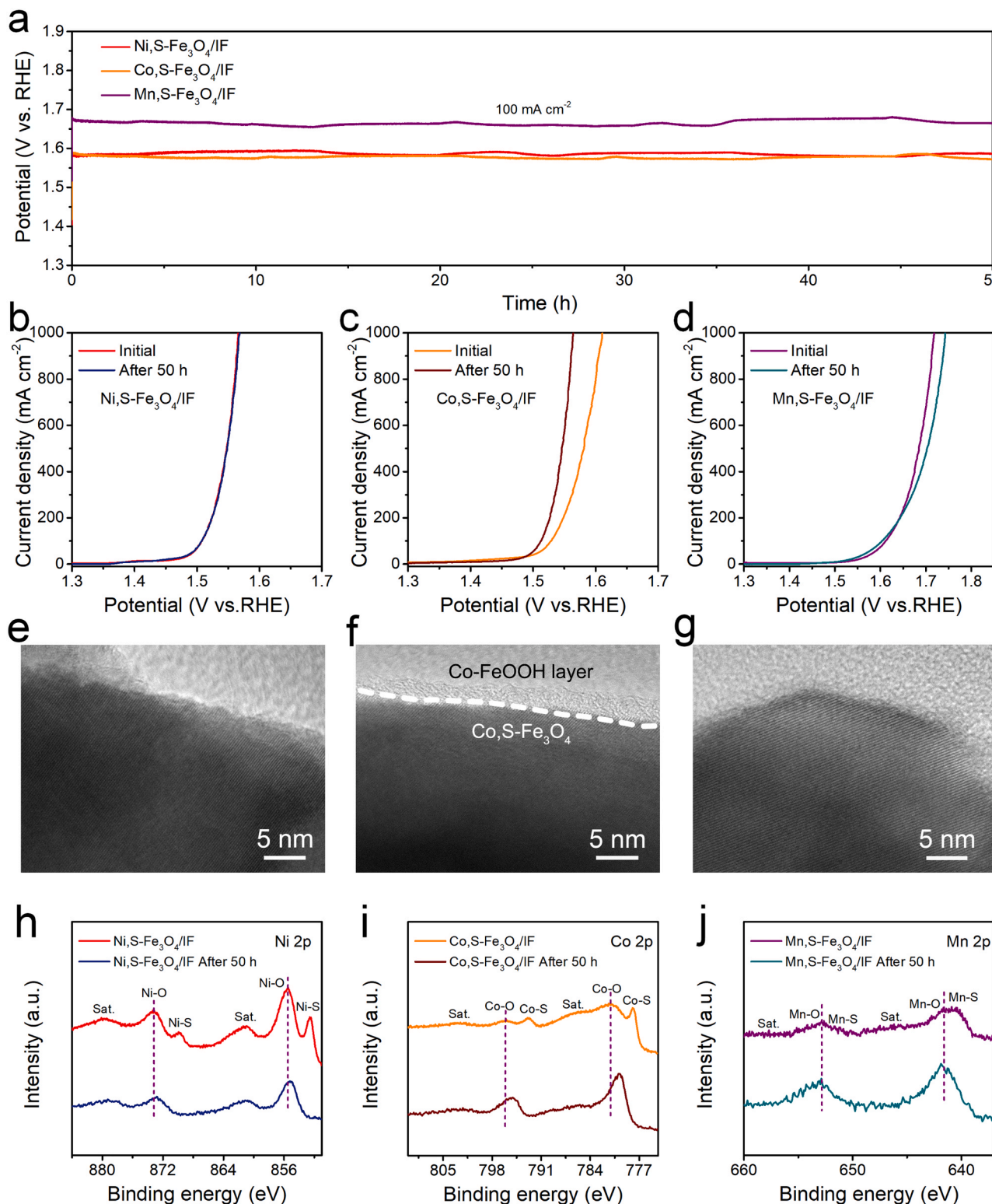


Fig. 6. a) Chronopotentiometric curves of $\text{Ni,S-Fe}_3\text{O}_4/\text{IF}$, $\text{Co,S-Fe}_3\text{O}_4/\text{IF}$ and $\text{Mn,S-Fe}_3\text{O}_4/\text{IF}$ tested at a fixed current densities of 50 mA cm^{-2} for 50 h without iR compensation. LSV curves of b) $\text{Ni,S-Fe}_3\text{O}_4/\text{IF}$, c) $\text{Co,S-Fe}_3\text{O}_4/\text{IF}$ and d) $\text{Mn,S-Fe}_3\text{O}_4/\text{IF}$ before and after the 50 h stability test. h) Ni 2p XPS spectra of $\text{Ni,S-Fe}_3\text{O}_4/\text{IF}$ and $\text{Ni,S-Fe}_3\text{O}_4/\text{IF}$ after the 50 h stability test. i) Co 2p XPS spectra of $\text{Co,S-Fe}_3\text{O}_4/\text{IF}$ and $\text{Co,S-Fe}_3\text{O}_4/\text{IF}$ after the 50 h stability test. j) Mn 2p XPS spectra of $\text{Mn,S-Fe}_3\text{O}_4/\text{IF}$ and $\text{Mn,S-Fe}_3\text{O}_4/\text{IF}$ after the 50 h stability test.

the fundamental mechanism of the excellent durability and reveal the phase changes during OER processes, SEM, XRD and XPS characterizations of the post-OER $\text{M,S-Fe}_3\text{O}_4/\text{IF}$ have been implemented (Fig. S23-26). As shown in SEM images of Fig. S23, the overall nanosheet morphologies remain unchanged, and the surface of nanosheets in post-OER

$\text{Co,S-Fe}_3\text{O}_4/\text{IF}$ becomes rougher, which may be related to the surface reconstruction of $\text{Co,S-Fe}_3\text{O}_4$ nanosheets during the OER process of 50 h (Fig. S23b). The crystal structures of $\text{M,S-Fe}_3\text{O}_4/\text{IF}$ after the stability test remain almost unchanged, as shown in XRD results (Fig. S24). It worth noting that, the unchanged XRD peaks confirm that the reconstruction of

Co,S-Fe₃O₄/IF has only occurred on the surface of original precatalyst. This can also be verified by the results of TEM tests on the post-OER samples. In contrast to TEM results of post-OER Ni,S-Fe₃O₄/IF and Mn,S-Fe₃O₄/IF samples (Figs. 6e and 6g), an oxyhydroxide layer with a different contrast can be observed on the surface of Co,S-Fe₃O₄ nano-sheets in the post-OER Co,S-Fe₃O₄/IF sample (Fig. 6f).

XPS tests were performed to analyse changes of surface chemical states in M,S-Fe₃O₄/IF after 50 h OER processes (Fig. S25-26). The S 2p signals in the XPS survey spectra of M,S-Fe₃O₄/IF have vanished after 50 h OER process (Fig. S26c, S26f, and S26i), and K 2s and K 2p signals are remarkably obvious in the Fig. S25 [54], which originate from the in situ electrochemical oxidizing of M,S-Fe₃O₄/IF in 1.0 M KOH solution at a constant current density of 100 mA cm⁻² for 50 h. XPS analyses of Fe 2p spectra (Fig. S26a, S26d, and S26g) exhibit negative shifts of peaks owing to the S leaching in the long-term oxygen evolution process [46]. By comparing the O 1s spectra before and after the 50 h stability test, it can be found that the M-OH specie on the surface of Co,S-Fe₃O₄/IF increases most significantly after the stability test, which is consistent with its surface reconstruction to form FeOOH. As for Ni 2p, Co 2p, and Mn 2p spectra (Figs. 6h, 6i, and 6j), after the OER process, it is noteworthy that the Ni-S, Co-S and Mn-S peaks have also vanished in the XPS via in situ electrochemical oxidizing process in 1.0 M KOH. In particular, after the 50 h stability test, the Ni-O and Mn-O bonds show no significant change, while the Co-O bond moves significantly in the direction of lower

binding energy, indicating that the valence states of Ni and Mn are essentially unchanged after the stability test, while the valence state of Co increases significantly, which is consistent with the surface reconstruction process of a Co-FeOOH layer on the Co,S-Fe₃O₄/IF surface.

In order to better elucidate the changes on the surfaces of the catalysts, Ni 2p, Co 2p, and Mn 2p XPS spectra of M,S-Fe₃O₄/IF after 50 h OER processes were collected after the etching of 10 and 50 nm (Fig. S27). It can be found that, after the etching of 10 nm, Ni-S and Mn-S signals start to reappear, while the Co-S signal is still missing. After the etching of 50 nm, Ni 2p, Co 2p, and Mn 2p spectra of the samples are almost the same as the initial XPS spectra of the Fe₃O₄-based samples. The M-S signals disappearing after the stability test reappear, and the shifts of M-O signals are recovered in the Ni 2p, Co 2p, and Mn 2p spectra. This indicates that the structural changes of the catalyst during the stability test occur only in the surface layer. Compared to Ni,S-Fe₃O₄/IF and Mn,S-Fe₃O₄/IF, Co,S-Fe₃O₄/IF has a more obvious and deeper surface reconstruction process, which is consistent with the TEM result in Fig. 6f. The Co,S-Fe₃O₄ surface reconstructs to form a Co-doped FeOOH layer, whereas the Ni,S-Fe₃O₄ and Mn,S-Fe₃O₄ surfaces are left with only S vacancies after S leaching and do not form a significant FeOOH layer. For Co system, the formation of the Co-doped FeOOH layer results in an enhanced OER activity, thanks to the activated OER under the LOM pathway of the sample. In contrast, for Ni and Mn systems, S vacancies can act as an electronic regulator similar to the

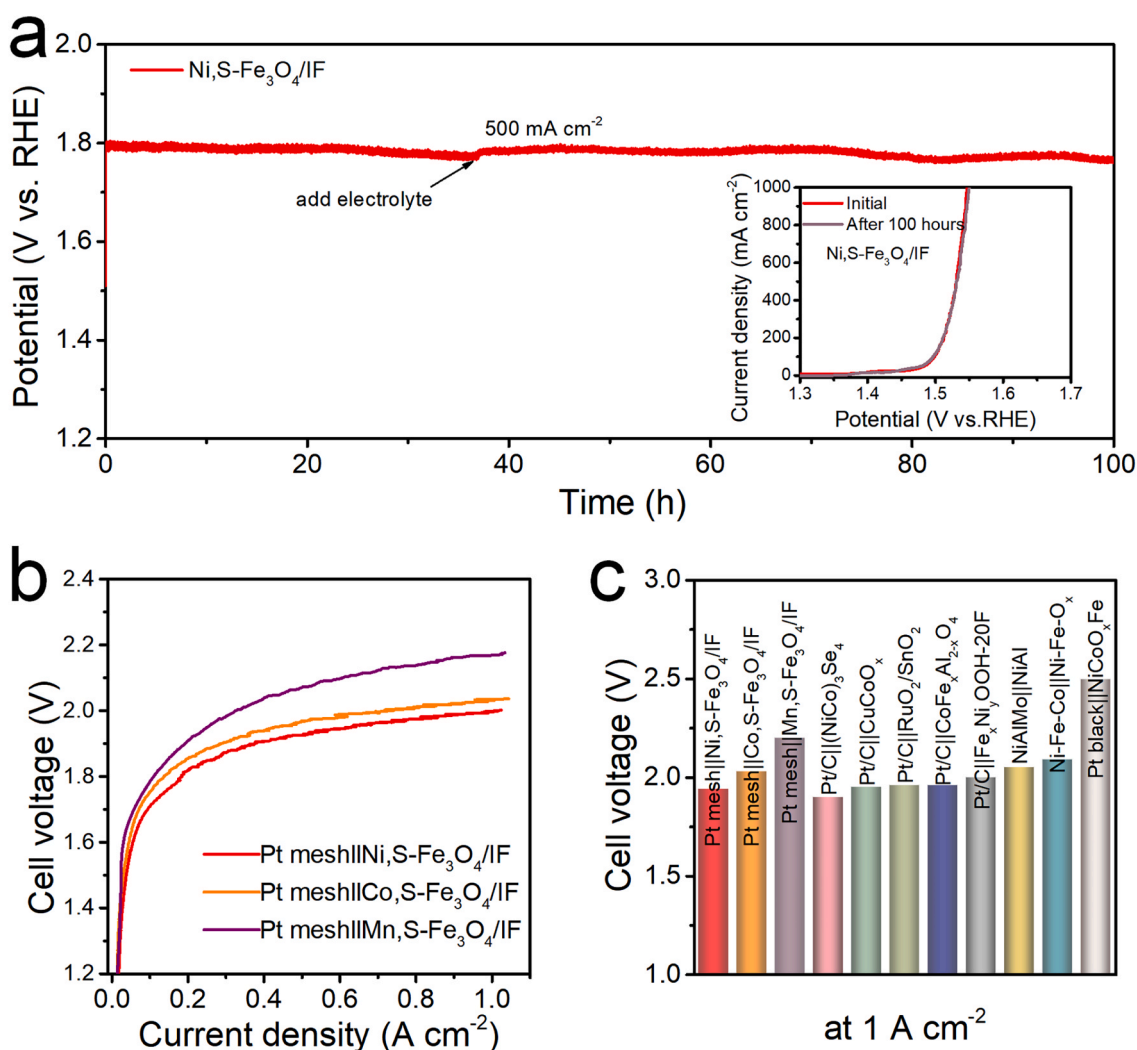


Fig. 7. a) Stability test of Ni,S-Fe₃O₄/IF at current density of 500 mA cm⁻², and the inset are LSV curves of Ni,S-Fe₃O₄/IF before and after the 100 h stability test. b) The polarization curves of AEMWE in 1.0 M KOH at 60 °C. c) Comparison cell voltages of catalysts in the MEA configuration at 1.0 A cm⁻².

heterogeneous S atom with lower electronegativity, allowing the OER activity of the sample to be maintained. To better investigate the rate of S leaching from Fe-based catalysts during OER, the elemental concentrations of S in the electrolyte solution were investigated by Inductively Coupled Plasma Optical Emission Spectrometer (ICP-OES). As exhibited in Fig. S28, the S concentration in the electrolyte first increases and then stabilizes. These indicates that S atoms in the surface region of the catalysts undergo leaching during the initial stage of the electrocatalytic stability test, causing the reconstruction of catalysts or the formation of oxygen vacancies. Notably, all of S leaching processes for obtained Fe-based catalysts exhibit self-termination characteristics, favorable to the construction of a stable catalytic interface.

We further tested the stability of the Ni,S-Fe₃O₄/IF catalyst at an industrial high current density of 500 mA cm⁻² for 100 h (Fig. 7a). The catalyst was also found to be stable against this industrially OER environment (insert of the Fig. 7a). To further evaluate the performance of Ni,S-Fe₃O₄/IF, Co,S-Fe₃O₄/IF and Mn,S-Fe₃O₄/IF as OER

electrocatalysts for the industrial water splitting, we have integrated our electrocatalysts into membrane-electrode-assembly (MEA) to assemble an alkaline anion exchange membrane water electrolyzer (AEMWE) device, as shown in the Fig. S29. Fig. 7b displays the water-splitting performance of the Pt mesh||M,S-Fe₃O₄/IF AEMWE setup operating in 1.0 M KOH at 60 °C. In line with their catalytic activity in the typical three-electrode system, the efficiencies of electrolyzers follow the order of Pt mesh||Ni,S-Fe₃O₄/IF > Pt mesh||Co,S-Fe₃O₄/IF > Pt mesh||Mn,S-Fe₃O₄/IF. The most excellent AEMWE device, a Pt mesh||Ni,S-Fe₃O₄/IF cathode/anode configuration, can deliver up to 1 A cm⁻² at the cell voltage of 1.94 V at 60 °C. In addition, the above performance in the AEMWE is comparable and even superior to that of transition metal electrocatalysts reported under similar conditions (Fig. 7c) [47–54], demonstrating the potential of Ni,S-Fe₃O₄/IF for industrial applications.

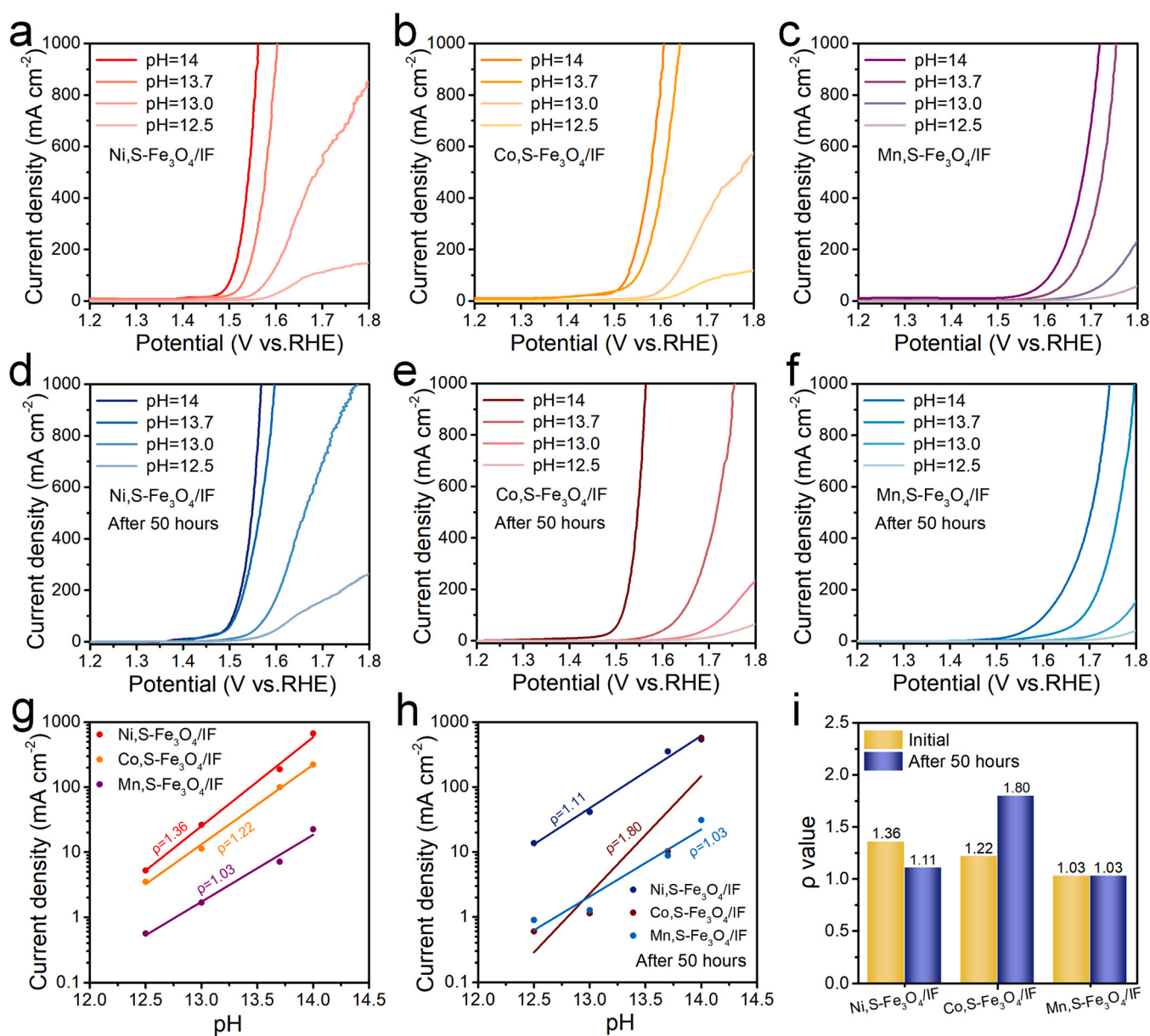


Fig. 8. LSV curves of a) Ni,S-Fe₃O₄/IF, b) Co,S-Fe₃O₄/IF, c) Mn,S-Fe₃O₄/IF, and d) Ni,S-Fe₃O₄/IF after 50 h, e) Co,S-Fe₃O₄/IF after 50 h, f) Mn,S-Fe₃O₄/IF after 50 h under different pHs. g,h) Current densities of initial samples and after 50 h at 1.55 V versus RHE as a function of the pH value. The proton reaction orders of the catalysts were obtained by using the following equation: $\rho = (\partial \log(i) / \partial \text{pH})$. i) The proton reaction orders of the initial catalysts and after 50 h.

3.3. Insights into the oxygen evolution mechanism

For OER processes on the metal sites of transition metal oxide surface, the adsorbate evolution mechanism (AEM) and lattice oxygen mechanism (LOM) involving four coordinated proton-electron transfer steps have been reported [55–57]. In general, for the OER process under LOM, a mismatch between the electron transfer dynamics and the hydroxy affinity at the interface between catalysts and electrolyte causes a pH-dependent OER activity. In order to investigate the feasibility of LOM, the M,S-Fe₃O₄/IF samples before and after the 50 h stability test were monitored in a series of KOH electrolytes with pH of 12.5–14. For all M,S-Fe₃O₄/IF samples before and after the 50 h stability test, the current densities show a different degree of increase with the increasing pH (Fig. 8a–f). For M,S-Fe₃O₄/IF samples before the 50 h stability test, at 1.55 V (vs. RHE), the increased current density of Ni,S-Fe₃O₄/IF and Co,S-Fe₃O₄/IF are significantly higher than that of Mn,S-Fe₃O₄/IF (Fig. 8c) and Fe₃O₄/IF (Fig. S30), revealing that Ni,S-Fe₃O₄/IF and Co,S-Fe₃O₄/IF exhibit stronger pH-dependent OER activities and more pronounced lattice-oxygen involvement. Moreover, proton reaction orders on the RHE scale have been obtained from the slopes (ρ) in Fig. 8g [43,58]. The slope of Ni,S-Fe₃O₄/IF and Co,S-Fe₃O₄/IF (1.36 and 1.22 decade pH⁻¹) is larger than that of Mn,S-Fe₃O₄/IF and Fe₃O₄/IF, suggesting that the nonconcerted proton-electron transfer process for OER can be prompted on the surface of Ni,S-Fe₃O₄/IF and Co,S-Fe₃O₄/IF, and this also proves that Ni,S-Fe₃O₄/IF and Co,S-Fe₃O₄/IF follows prefer to follow the LOM pathway rather than the AEM pathway in OER processes [55,59]. However, for M,S-Fe₃O₄/IF samples after the 50 h stability test, it is surprising to find that the post-OER Ni,S-Fe₃O₄/IF shows a lower ρ value and the post-OER Co,S-Fe₃O₄/IF shows a higher ρ value, which indicates that Ni,S-Fe₃O₄/IF with the S leaching is more conducive to the AEM in the OER process, and the reconstructed Co-FeOOH layer in Co,S-Fe₃O₄/IF is more conducive to the LOM in the OER process (Fig. 8h,i).

In order to better elaborate the OER reaction mechanism of the Fe-based catalysts involved in this work, DFT calculations were performed. Based on previous reports on transition metal oxide OER catalysts, both typical OER mechanisms such as AEM and LOM on the surface of Fe based oxide catalysts were simulated. In the AEM mechanism containing *OH, *OOH, and *O intermediates, it can be found that the introduction of heterogeneous atoms can modulate the adsorption free energy of OER reaction intermediates. Among them, the co-doping strategy of M and S is more obvious for the regulation of the adsorption free energy of the OER reaction intermediates, where the Ni,S-Fe₃O₄ model presents the most excellent rate-determining step (RDS) barrier of only 0.28 eV (Fig. 9a,b), which is better than the Co,S-Fe₃O₄ (0.31 eV), Mn,S-Fe₃O₄ (0.93 eV), Ni-Fe₃O₄ (2.31 eV), Co-Fe₃O₄ (2.43 eV), Mn-Fe₃O₄ (1.95 eV), S-Fe₃O₄ (0.89 eV), and Fe₃O₄ (0.99 eV) models. With the participation of lattice oxygen, the LOM pathway on the surface of the Fe-based oxide catalyst contains reaction intermediates differing from the AEM mechanism. The introduction of heterogeneous atoms can modulate the redox activity of lattice oxygen. Similarly, the co-doping strategy of M and S is more effective in regulating the redox activity of lattice oxygen, where the Ni,S-Fe₃O₄ model presents the most excellent RDS barrier of only 0.62 eV (Fig. 9c,d), which is better than the Co,S-Fe₃O₄ (0.67 eV), Mn,S-Fe₃O₄ (1.0 eV), Ni-Fe₃O₄ (2.68 eV), Co-Fe₃O₄ (1.88 eV), Mn-Fe₃O₄ (1.97 eV), S-Fe₃O₄ (2.59 eV), and Fe₃O₄ (1.07 eV) models. For all the OER processes presented on the surface of the Fe-based oxide catalysts, the RDS barrier presented in the AEM or LOM pathways can alone serve as a descriptor for the theoretical overpotential, but only shows a weak correlation with the actual overpotential (Fig. 9e). Therefore, it can be supposed that OER processes on the surfaces of Fe-based oxide catalysts should involve different proportions of AEM and LOM, simultaneously. As shown in Fig. 9f, the correlation between the theoretical overpotential and the actual overpotential increases dramatically when the mixed mechanism including

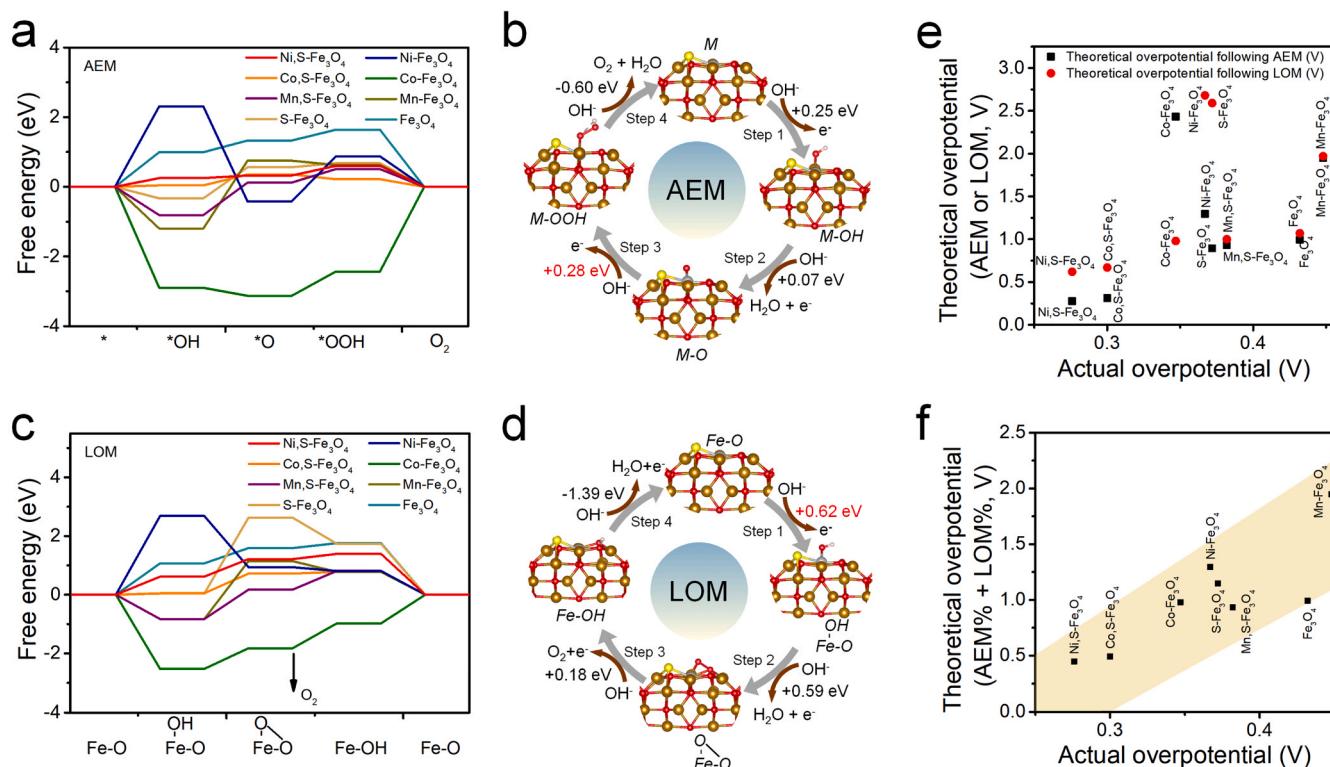


Fig. 9. Gibbs free energy diagram for OER on M,S-Fe₃O₄, M-Fe₃O₄, S-Fe₃O₄, and Fe₃O₄ surface at 1.23 V based on a) AEM and c) LOM mechanism. The optimized structures of OER intermediates on the Ni,S-Fe₃O₄ from the side view based on b) AEM mechanism and d) LOM mechanism. e) Theoretical overpotential of M,S-Fe₃O₄, M-Fe₃O₄, S-Fe₃O₄, and Fe₃O₄ surface at 1.23 V based on AEM or LOM mechanism. f) Theoretical overpotential of M,S-Fe₃O₄, M-Fe₃O₄, S-Fe₃O₄, and Fe₃O₄ surface at 1.23 V based on AEM and LOM mechanism. (Brown ball: Fe atom; red ball: O atom; yellow ball: S atom; gray ball: Ni atom; pink ball: H atom).

AEM and LOM as set in Table S2 are adopted, suggesting that the mixed AEM and LOM pathways can better predict the actual OER activities of the Fe-based oxide catalysts. In fact, the proportions of AEM and LOM set by Table S2 are only one possible case for OER processes on the surfaces of Fe-based oxide catalysts, and the proportions between AEM and LOM can be adjusted within a certain range. Thus, the mixed

mechanism including AEM and LOM better provides flexibility for the prediction of OER activities of Fe-based oxide catalysts. Specifically, the mixed AEM and LOM mechanism can better explain the weakened LOM of the Ni,S-Fe₃O₄ catalyst after the actual stability test, which is due to the increased proportion of AEM on the surface of the Ni,S-Fe₃O₄ catalyst after the actual stability test.

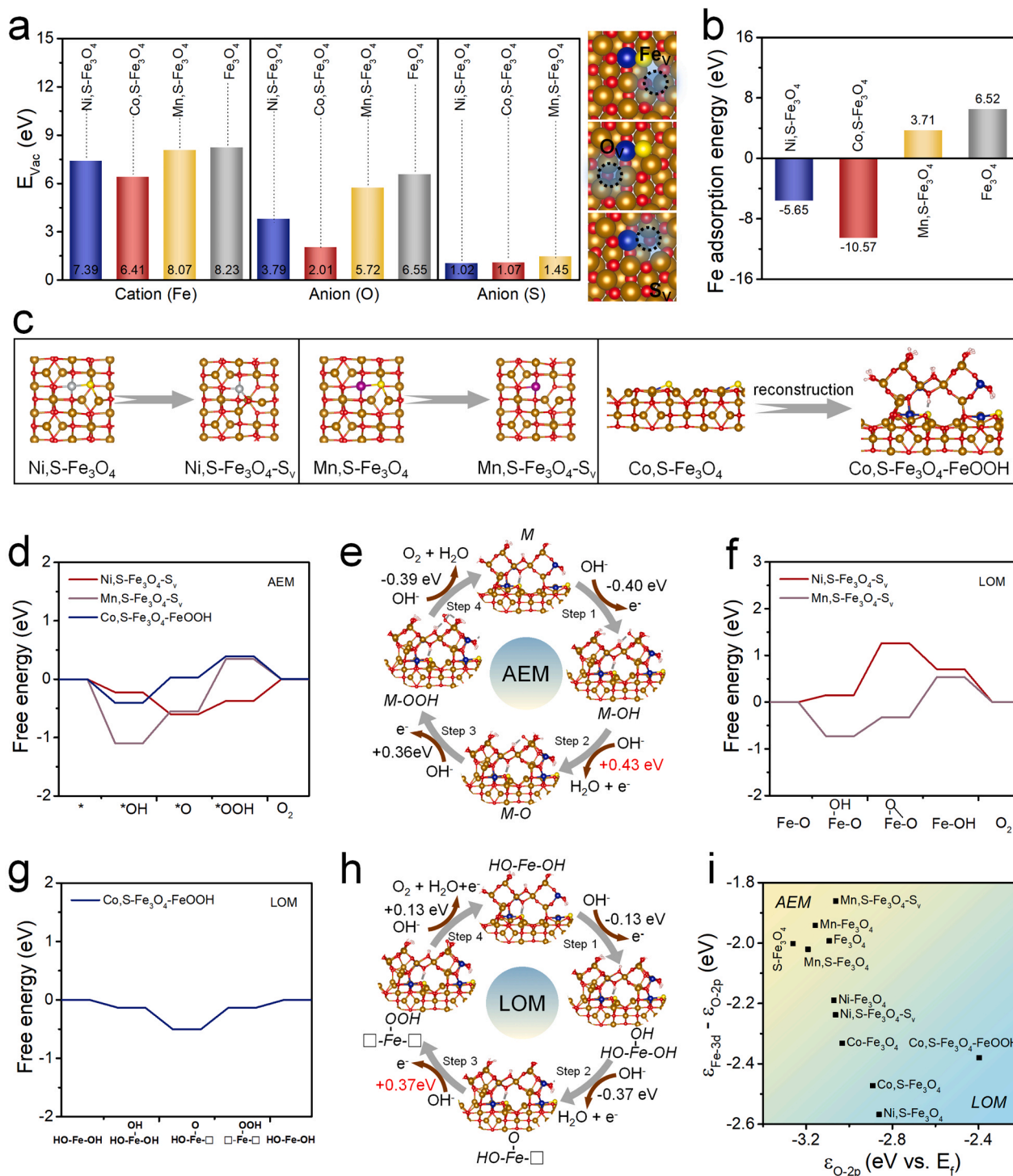


Fig. 10. a) Vacancy formation energies of cation (Fe), and anions (O and S). b) Fe adsorption energies. c) The schematic illustration of structural evolution for Ni,S-Fe₃O₄, Mn,S-Fe₃O₄ and Co,S-Fe₃O₄. d) Gibbs free energy diagram for OER on Ni,S-Fe₃O₄-S_v, Mn,S-Fe₃O₄-S_v, Co,S-Fe₃O₄-FeOOH surface at 1.23 V based on AEM mechanism. The optimized structures of OER intermediates on the Co,S-Fe₃O₄-FeOOH from the side view based on e) AEM and h) LOM mechanism. f) Gibbs free energy diagram for OER on Ni,S-Fe₃O₄-S_v and Mn,S-Fe₃O₄-S_v surface at 1.23 V based on LOM mechanism. g) Gibbs free energy diagram for OER on Co,S-Fe₃O₄-FeOOH surface at 1.23 V based on LOM mechanism. i) The relationship between the OER mechanism (AEM and LOM) and electronic descriptors for various electrocatalysts. (Brown ball: Fe atom; red ball: O atom; yellow ball: S atom; gray ball: Ni atom; blue ball: Co atom; purple ball: Mn atom; pink ball: H atom).

To better elucidate the changes in the surface of the M,S-Fe₃O₄ catalyst in electrochemical tests, the vacancy formation energies of the anions and cations contained in the M,S-Fe₃O₄ catalyst were calculated separately by DFT. It can be clearly shown that M and S co-doping has a significant change on the vacancy formation energy of anions and cations on the surfaces of Fe₃O₄ (Fig. 10a). Compared to Fe₃O₄, M,S-Fe₃O₄ models present lower vacancy formation energies for Fe cations and O anions. Among the M,S-Fe₃O₄ surfaces, the Co,S-Fe₃O₄ surface presents the lowest vacancy formation energy of Fe cations ($E_{\text{Fe-vac}}$, 6.41 eV) and O anions ($E_{\text{O-vac}}$, 2.01 eV), which implies that the dissolution of Fe cations and O anions is easier on the Co,S-Fe₃O₄ surface, consistent with weakened Co-O bonds shown by the XPS results in Fig. 3b. By comparing the vacancy formation energy among Fe, O, and S, it can be found that the vacancy formation energy of S anions on the surface of the M,S-Fe₃O₄ model is overall smaller than that of Fe cations and O anions, which indicates that the dissolution of S anions is more spontaneous on the surface of M,S-Fe₃O₄. The Fe deposition, an important behavior in the electrochemical reconstruction process, has also been simulated by DFT calculations. It can be found that the surface of the Co,S-Fe₃O₄ model presents the lowest Fe deposition energy (−10.57 eV) (Fig. 10b), thanks to the promotion of Co for Fe deposition [23,35]. In summary of the above presented data on vacancy formation energy and Fe deposition energy, the surface changes of M,S-Fe₃O₄ catalysts after stability tests can be well interpreted (Fig. 10c): M,S-Fe₃O₄ catalysts first undergo the process of the S leaching in electrochemical tests, and since the dissolution of Fe and O, and Fe deposition on the surfaces of Ni,S-Fe₃O₄ and Mn,S-Fe₃O₄ are more difficult, Ni,S-Fe₃O₄ and Mn,S-Fe₃O₄ catalysts only transform into Ni,S-Fe₃O₄ and Mn,S-Fe₃O₄ catalysts with S vacancies (Ni,S-Fe₃O₄-S_v and Mn,S-Fe₃O₄-S_v); while Fe ions on the surface of Co,S-Fe₃O₄ can be dissolved into the electrolyte under the promotion of the S leaching, gradually deposited onto the surface of Co,S-Fe₃O₄ in the subsequent electrochemical test under the promotion of the Co component, and then form a heterogeneous structure composed of Co, S-Fe₃O₄ and FeOOH (Co,S-Fe₃O₄-FeOOH).

The OER reactions on Ni,S-Fe₃O₄-S_v, Mn,S-Fe₃O₄-S_v, and Co,S-Fe₃O₄-FeOOH surfaces under AEM and LOM pathways were also simulated. Under the AEM pathway, OER processes on the Ni,S-Fe₃O₄-S_v, Mn,S-Fe₃O₄-S_v, and Co,S-Fe₃O₄-FeOOH surfaces are same as those on the corresponding Ni,S-Fe₃O₄, Mn,S-Fe₃O₄, and Co,S-Fe₃O₄ surfaces, showing similar RDS barriers, respectively (Fig. 10d). This is due to the fact that the S_v and OH coordinations play a similar electronic regulatory role to the initial S coordination. Under the LOM pathway, OER processes on the Ni,S-Fe₃O₄-S_v and Mn,S-Fe₃O₄-S_v surfaces include different reaction intermediates from those on the Co,S-Fe₃O₄-FeOOH surface due to the difference in the dehydrogenation steps (Fig. 10e-h). By comparing the differences of OER processes under the LOM pathway on the initial and final surfaces, it can be found that the S leaching makes OER processes under LOM relatively suppressed for Ni,S-Fe₃O₄-S_v and Mn,S-Fe₃O₄-S_v surfaces, while the electrochemical reconstruction makes the OER process under LOM of Co,S-Fe₃O₄-FeOOH surface promoted, which is consistent with the results of the change of electrochemical response under different pH electrolytes before and after the stability test.

To promote the participation of lattice oxygen in the OER process, the energy level of the O 2p and Fe 3d also needs to be regulated (Fig. S31 and S32). Ideally, the absolute energy level of $\varepsilon_{\text{O-2p}}$ versus Fermi level (E_{F}) needs to be high enough to allow activated lattice oxygen atoms to release from the lattice matrix [57]. Taking this into account, it can be inferred that both the relative energy relationship between Fe 3d and O 2p orbitals and the absolute energy level of the O 2p orbital have a decisive effect on the OER mechanism, and should be carefully investigated to explore the OER pathway following AEM or LOM. The good determination of the OER mechanism matching with the actual OER performance can be supported by the comprehensive DOS calculations of Fe-based electrocatalysts. As illustrated in Fig. 10i, Fe-based electrocatalysts via AEM are located in the left-top regions with

relatively high $\varepsilon_{\text{Fe-3d}}-\varepsilon_{\text{O-2p}}$ and low $\varepsilon_{\text{O-2p}}$ values, and Fe-based electrocatalysts via LOM are located in the right-bottom regions with relatively low $\varepsilon_{\text{Fe-3d}}-\varepsilon_{\text{O-2p}}$ and high $\varepsilon_{\text{O-2p}}$ values.

4. Conclusions

In summary, by combining theoretical calculations with experimental characterizations, we have successfully prepared a series of catalysts of M (M = Ni, Co, Mn) and S co-doped Fe₃O₄ nanosheets as OER catalysts by a facile hydrothermal strategy. The interconnected array of nanosheets provides numerous catalytically active sites and buffers the large volume changes during the electrochemical process. The introduction of M and S atoms into the Fe₃O₄ lattice causes the lattice distortion and the electronic modulation, and thus affects the OER performance of Fe₃O₄. As expected, benefiting from the structural and compositional advantages, the obtained Ni,S-Fe₃O₄/IF manifest a superior electrocatalytic performance towards OER in alkaline media, outputting the lowest overpotential of 312 mV to achieve an industrial high current density of 500 mA cm^{−2} and maintaining 100 h. The most excellent AEMWE device integrating Ni,S-Fe₃O₄/IF can deliver up to 1 A cm^{−2} at the cell voltage of 1.94 V at 60 °C. Particularly, among M,S-Fe₃O₄/IF samples, only Co,S-Fe₃O₄/IF undergoes a significant surface reconstruction with the overpotential improvement of 18 mV at 100 mA cm^{−2} during the long stability test, which reveals the important role of the Co component in electrochemical reconstructions of Fe₃O₄ involving Fe dissolution and Fe redeposition during alkaline OER. In addition, a mixed OER mechanism including both AEM and LOM proposed can achieve a better match theoretical OER performance with experimental OER performance of Fe-based inverse spinel oxides. The findings here open a new perspective in the fundamental and comprehensive understanding of electronic modulations, lattice distortions, and surface reconstruction under mixed OER mechanisms for spinel electrocatalysts.

CRedit authorship contribution statement

Hai-Jun Liu: Data curation, Writing – original draft, Formal analysis, Investigation, Writing – review & editing. **Shuo Zhang:** Writing – original draft, Conceptualization, Formal analysis, Writing – review & editing. **Ruo-Yao Fan:** Writing – review & editing, Formal analysis. **Bin Liu:** Writing – original draft, Methodology. **Ren-Qing Lv:** Writing – original draft, Formal analysis. **Yong-Ming Chai:** Funding acquisition, Conceptualization, Investigation, Resources, Formal analysis, Supervision, Writing – review & editing. **Bin Dong:** Formal analysis, Investigation, Resources, Writing – original draft, Funding acquisition, Project administration, Writing – review & editing.

Declaration of Competing Interest

The authors declare that they have no known competing financial interests or personal relationships that could have appeared to influence the work reported in this paper.

Data Availability

Data will be made available on request.

Acknowledgements

This work is financially supported by National Natural Science Foundation of China (52174283 and 52274308).

Appendix A. Supporting information

Supplementary data associated with this article can be found in the online version at doi:10.1016/j.apcatb.2023.123567.

References

- [1] Y. Sun, H. Liao, J. Wang, B. Chen, S. Sun, S.J.H. Ong, S. Xi, C. Diao, Y. Du, J. O. Wang, M.B.H. Breese, S. Li, H. Zhang, Z.J. Xu, Covalency competition dominates the water oxidation structure–activity relationship on spinel oxides, *Nat. Catal.* 2 (2020) 554–563.
- [2] R.Y. Fan, X.J. Zhai, W.Z. Qiao, Y.S. Zhang, N. Yu, Y.M. Chai, B. Dong, Optimized electronic modification of S-Doped CuO induced by oxidative reconstruction for coupling glycerol electrooxidation with hydrogen, *Evol., Nano-Micro Lett.* 15 (2023) 190.
- [3] Y.N. Zhou, Y.W. Dong, Y. Wu, B. Dong, H.J. Liu, X.J. Zhai, G.Q. Han, D.P. Liu, Y. M. Chai, Nitrate induced precise atom substitution and vacancies for overall water splitting, *Chem. Eng. J.* 463 (2023), 142380.
- [4] L. Li, G. Zhang, B. Wang, S. Yang, Constructing the Fe/Cr double (oxy)hydroxides on Fe₃O₄ for boosting the electrochemical oxygen evolution in alkaline seawater and domestic sewage, *Appl. Catal. B Environ.* 302 (2022), 120847.
- [5] X. Li, Q. Hu, H. Yang, T. Ma, X. Chai, C. He, Bimetallic two-dimensional materials for electrocatalytic oxygen evolution, *Chin. Chem. Lett.* 33 (2022) 3657–3671.
- [6] R. He, C. Wang, L. Feng, Amorphous FeCoNi-S as efficient bifunctional electrocatalysts for overall water splitting reaction, *Chin. Chem. Lett.* 34 (2023), 107241.
- [7] J. Zhu, J. Qian, X. Peng, B. Xia, D. Gao, Etching-induced surface reconstruction of NiMoO₄ for oxygen evolution reaction, *Nano-Micro Lett.* 15 (2023) 30.
- [8] Q. Zhou, C. Xu, J. Hou, W. Ma, T. Jian, S. Yan, H. Liu, Duplex interpenetrating-phase FeNiZn and FeNi₃ heterostructure with low-gibbs free energy interface coupling for highly efficient overall water splitting, *Nano-Micro Lett.* 15 (2023) 95.
- [9] W. Wang, Z. Wang, Y. Hu, Y. Liu, S. Chen, A potential-driven switch of activity promotion mode for the oxygen evolution reaction at Co₃O₄/NiOxHy interface, *eScience* 2 (2022) 438–444.
- [10] F. Meng, C. Dai, Z. Liu, S. Luo, J. Ge, Y. Duan, G. Chen, C. Wei, R.R. Chen, J. Wang, D. Mandler, Z.J. Xu, Methanol electro-oxidation to formate on iron-substituted lanthanum cobaltite perovskite oxides, *eScience* 2 (2022) 87–94.
- [11] H. Lei, L. Ma, Q. Wan, S. Tan, B. Yang, Z. Wang, W. Mai, H.J. Fan, Promoting surface reconstruction of NiFe layered double hydroxide for enhanced oxygen evolution, *Adv. Energy Mater.* 12 (2022) 2202522.
- [12] H.J. Liu, R.N. Luan, L.Y. Li, R.Q. Lv, Y.M. Chai, B. Dong, Sulphur-dopant induced breaking of the scaling relation on low-valence Ni sites in nickel ferrite nanorods for water oxidation with industrial-level current density, *Chem. Eng. J.* 461 (2023), 141714.
- [13] Y.N. Zhou, F.L. Wang, S.Y. Dou, Z.N. Shi, B. Dong, W.L. Yu, H.Y. Zhao, F.G. Wang, J.F. Yu, Y.M. Chai, Motivating high-valence Nb doping by fast molten salt method for NiFe hydroxides toward efficient oxygen evolution reaction, *Chem. Eng. J.* 427 (2022), 131643.
- [14] A. Badreldin, J. Abed, N. Hassan, A. El-Ghenymy, W. Suwaileh, Y. Wubulikasimu, Z.K. Ghouri, K. Youssef, D. Kumar, K. Elsaid, E.H. Sargent, A. Abdel-Wahab, Sulfide interlayered cobalt-based oxytrifides for efficient oxygen evolution reaction in neutral pH water and seawater, *Appl. Catal. B Environ.* 330 (2023), 122599.
- [15] H.-Y. Jeong, J. Oh, G.S. Yi, H.-Y. Park, S.K. Cho, J.H. Jang, S.J. Yoo, H.S. Park, High-performance water electrolyzer with minimum platinum group metal usage: Iron nitride-iridium oxide core-shell nanostructures for stable and efficient oxygen evolution reaction, *Appl. Catal. B Environ.* 330 (2023), 122596.
- [16] G. Liu, R. Yao, Y. Zhao, M. Wang, N. Li, Y. Li, X. Bo, J. Li, C. Zhao, Encapsulation of Ni/Fe₃O₄ heterostructures inside onion-like N-doped carbon nanorods enables synergistic electrocatalysis for water oxidation, *Nanoscale* 10 (2018) 3997–4003.
- [17] Z.J. Xu, Transition metal oxides for water oxidation: all about oxyhydroxides? *Sci. China Mater.* 63 (2019) 3–7.
- [18] J. Jin, J. Yin, H. Liu, B. Huang, Y. Hu, H. Zhang, M. Sun, Y. Peng, P. Xi, C.H. Yan, Atomic sulfur filling oxygen vacancies optimizes H₂ absorption and boosts the hydrogen evolution reaction in alkaline media, *Angew. Chem. Int. Ed.* 60 (2021) 14117–14123.
- [19] R.Y. Fan, Y.N. Zhou, M.X. Li, J.Y. Xie, W.L. Yu, J.Q. Chi, L. Wang, J.F. Yu, Y. M. Chai, B. Dong, In situ construction of Fe(Co)OOH through ultra-fast electrochemical activation as real catalytic species for enhanced water oxidation, *Chem. Eng. J.* 426 (2021), 131943.
- [20] Y. Li, G. Chen, Y. Zhu, Z. Hu, T.S. Chan, S. She, J. Dai, W. Zhou, Z. Shao, Activating both basal plane and edge sites of layered cobalt oxides for boosted water oxidation, *Adv. Funct. Mater.* 31 (2021) 2103569.
- [21] S. Han, S. Liu, S. Yin, L. Chen, Z. He, Electrodeposited Co-doped Fe₃O₄ thin films as efficient catalysts for the oxygen evolution reaction, *Electrochim. Acta* 210 (2016) 942–949.
- [22] X.-Y. Zhang, F.-T. Li, R.-Y. Fan, J. Zhao, B. Dong, F.-L. Wang, H.-J. Liu, J.-F. Yu, C.-G. Liu, Y.-M. Chai, F. P double-doped Fe₃O₄ with abundant defect sites for efficient hydrogen evolution at high current density, *J. Mater. Chem. A* 9 (2021) 15836–15845.
- [23] H.J. Liu, S. Zhang, Y.N. Zhou, W.L. Yu, Y. Ma, S.T. Wang, Y.M. Chai, B. Dong, Dynamically stabilized electronic regulation and electrochemical reconstruction in Co and S atomic pair doped Fe₃O₄ for water oxidation, *Small* (2023), e2301255.
- [24] Z.P. Wu, H. Zhang, S. Zuo, Y. Wang, S.L. Zhang, J. Zhang, S.Q. Zang, X.W.D. Lou, Manipulating the local coordination and electronic structures for efficient electrocatalytic oxygen evolution, *Adv. Mater.* 33 (2021), e2103004.
- [25] G. Yang, J. Zhu, P. Yuan, Y. Hu, G. Qu, B.A. Lu, X. Xue, H. Yin, W. Cheng, J. Cheng, W. Xu, J. Li, J. Hu, S. Mu, J.N. Zhang, Regulating Fe-spin state by atomically dispersed Mn-N in Fe-N-C catalysts with high oxygen reduction activity, *Nat. Commun.* 12 (2021) 1734.
- [26] J. Luo, W.H. Guo, Q. Zhang, X.H. Wang, L. Shen, H.C. Fu, L.L. Wu, X.H. Chen, H. Q. Luo, N.B. Li, One-pot synthesis of Mn-Fe bimetallic oxide heterostructures as bifunctional electrodes for efficient overall water splitting, *Nanoscale* 12 (2020) 19992–20001.
- [27] M. Li, Y. Xiong, X. Liu, X. Bo, Y. Zhang, C. Han, L. Guo, Facile synthesis of electrospun MFe₂O₄ (M = Co, Ni, Cu, Mn) spinel nanofibers with excellent electrocatalytic properties for oxygen evolution and hydrogen peroxide reduction, *Nanoscale* 7 (2015) 8920–8930.
- [28] M. Chen, N. Kitiphatpiboon, C. Feng, Q. Zhao, A. Abudula, Y. Ma, K. Yan, G. Guan, Tuning octahedron sites in MnFe₂O₄ spinel by boron doping for highly efficient seawater splitting, *Appl. Catal. B Environ.* 330 (2023), 122577.
- [29] V. Dao, L.A. Cipriano, S.-W. Ki, S. Yadav, W. Wang, G. Di Liberto, K. Chen, H. Son, J.-K. Yang, G. Pacchioni, L.-H. Lee, 2D/2D Z-scheme-based α-Fe₂O₃@NGr heterojunction implanted with Pt single-atoms for remarkable photocatalytic hydrogen evolution, *Appl. Catal. B Environ.* 330 (2023), 122586.
- [30] K. Wang, R. Jin, Y. Liu, J. Ai, Z. Liu, X. Li, N. Li, Three-dimensional ordered macroporous NiFe₂O₄ self-supporting electrode with enhanced mass transport for high-efficiency oxygen evolution reaction, *ACS Appl. Energy Mater.* 4 (2020) 268–274.
- [31] X. Zhang, S. Liu, Y. Zang, R. Liu, G. Liu, G. Wang, Y. Zhang, H. Zhang, H. Zhao, Co/Co₉S₈@S,N-doped porous graphene sheets derived from S, N dual organic ligands assembled Co-MOFs as superior electrocatalysts for full water splitting in alkaline media, *Nano Energy* 30 (2016) 93–102.
- [32] J. Yang, G. Zhu, Y. Liu, J. Xia, Z. Ji, X. Shen, S. Wu, Fe₃O₄-decorated Co₉S₈ nanoparticles in situ grown on reduced graphene oxide: a new and efficient electrocatalyst for oxygen evolution reaction, *Adv. Funct. Mater.* 26 (2016) 4712–4721.
- [33] P. Sennu, M. Christy, V. Aravindan, Y.-G. Lee, K.S. Nahm, Y.-S. Lee, Two-dimensional mesoporous cobalt sulfide nanosheets as a superior anode for a li-ion battery and a bifunctional electrocatalyst for the Li-O₂ system, *Chem. Mater.* 27 (2015) 5726–5735.
- [34] L. Cao, Z. Li, K. Su, M. Zhang, B. Cheng, Rational design of hollow oxygen deficiency-enriched NiFe₂O₄@N/rGO as bifunctional electrocatalysts for overall water splitting, *J. Energy Chem.* 54 (2021) 595–603.
- [35] C. Feng, F. Wang, Z. Liu, M. Nakabayashi, Y. Xiao, Q. Zeng, J. Fu, Q. Wu, C. Cui, Y. Han, N. Shibata, K. Domen, I.D. Sharp, Y. Li, A self-healing catalyst for electrocatalytic and photoelectrochemical oxygen evolution in highly alkaline conditions, *Nat. Commun.* 12 (2021) 5980.
- [36] W. Zong, D. Rao, H. Guo, Y. Ouyang, Y.E. Miao, W. Wang, J. Wang, F. Lai, T. Liu, Gradient phosphorus-doping engineering and superficial amorphous reconstruction in NiFe₂O₄ nanoarrays to enhance the oxygen evolution electrocatalysis, *Nanoscale* 12 (2020) 10977–10986.
- [37] Y. Huang, J.-J. Wang, Y. Zou, L.-W. Jiang, X.-L. Liu, W.-J. Jiang, H. Liu, J.-S. Hu, Selective Se doping of NiFe₂O₄ on an active NiOOH scaffold for efficient and robust water oxidation, *Chin. J. Catal.* 42 (2021) 1395–1403.
- [38] Z. Shao, Q. Zhu, Y. Sun, Y. Zhang, Y. Jiang, S. Deng, W. Zhang, K. Huang, S. Feng, Phase-reconfiguration-induced NiS/NiFe₂O₄ composite for performance-enhanced zinc-air batteries, *Adv. Mater.* 34 (2022), e2110172.
- [39] C. Singh, A. Goyal, R. Malik, S. Bansal, S. Singhal, Envisioning the attachment of CdS nanoparticles on the surface of MFe₂O₄ (M = Zn, Co and Ni) nanocubes: Analysis of structural, optical, magnetic and photocatalytic properties, *J. Alloy Compd.* 695 (2017) 351–363.
- [40] O.M. Hemed, Electron spin resonance and cation distribution studies of the Co_{0.6}Zn_{0.4}Mn_xFe_{2-x}O₄ ferrite system, *J. Magn. Magn. Mater.* 251 (2002) 50–60.
- [41] J. Ge, R.R. Chen, X. Ren, J. Liu, S.J.H. Ong, Z.J. Xu, Ferromagnetic-antiferromagnetic coupling core-shell nanoparticles with spin conservation for water oxidation, *Adv. Mater.* 33 (2021), e2101091.
- [42] Z.-F. Huang, J. Song, Y. Du, S. Xi, S. Dou, J.M.V. Nsanzimana, C. Wang, Z.J. Xu, X. Wang, Chemical and structural origin of lattice oxygen oxidation in Co-Zn oxyhydroxide oxygen evolution electrocatalysts, *Nat. Energy* 4 (2019) 329–338.
- [43] Z.F. Huang, S. Xi, J. Song, S. Dou, X. Li, Y. Du, C. Diao, Z.J. Xu, X. Wang, Tuning of lattice oxygen reactivity and scaling relation to construct better oxygen evolution electrocatalyst, *Nat. Commun.* 12 (2021) 3992.
- [44] X. Guo, E. Song, W. Zhao, S. Xu, W. Zhao, Y. Lei, Y. Fang, J. Liu, F. Huang, Charge self-regulation in 1T'-MoS₂ structure with rich S vacancies for enhanced hydrogen evolution activity, *Nat. Commun.* 13 (2022) 5954.
- [45] W. Zhu, T. Zhang, Y. Zhang, Z. Yue, Y. Li, R. Wang, Y. Ji, X. Sun, J. Wang, A practical-oriented NiFe-based water-oxidation catalyst enabled by ambient redox and hydrolysis co-precipitation strategy, *Appl. Catal. B Environ.* 244 (2019) 844–852.
- [46] M. Yang, J.Y. Xie, W.L. Yu, Y.N. Cao, B. Dong, Y.N. Zhou, F.L. Wang, Q.Z. Li, Y. L. Zhou, Y.M. Chai, Fe(Co)OOH dynamically stable interface based on self-sacrificial reconstruction for long-term electrochemical water oxidation, *ACS Appl. Mater. Interfaces* 13 (2021) 17450–17458.
- [47] J. Abed, S. Ahmadi, L. Laverdure, A. Abdellah, C.P. O'Brien, K. Cole, P. Sobrinho, D. Sinton, D. Higgins, N.J. Mosey, S.J. Thorpe, E.H. Sargent, In situ formation of nano Ni-Co oxyhydroxide enables water oxidation electrocatalysts durable at high current densities, *Adv. Mater.* (2021), e2103812.
- [48] A. Lim, H.-j Kim, D. Henkensmeier, S. Jong Yoo, J. Young Kim, S. Young Lee, Y.-E. Sung, J.H. Jang, H.S. Park, A study on electrode fabrication and operation variables affecting the performance of anion exchange membrane water electrolysis, *J. Ind. Eng. Chem.* 76 (2019) 410–418.
- [49] J.Y. Lim, G. Rahman, S.Y. Chae, K.-Y. Lee, C.-S. Kim, O.-S. Joo, Highly stable RuO₂/SnO₂ nanocomposites as anode electrocatalysts in a PEM water electrolysis cell, *Int. J. Energy Res.* 38 (2014) 875–883.
- [50] T. Wu, S. Sun, J. Song, S. Xi, Y. Du, B. Chen, W.A. Sasangka, H. Liao, C.L. Gan, G. G. Scherer, L. Zeng, H. Wang, H. Li, A. Grimaud, Z.J. Xu, Iron-facilitated dynamic

- active-site generation on spinel CoAl_2O_4 with self-termination of surface reconstruction for water oxidation, *Nat. Catal.* 2 (2019) 763–772.
- [51] J. Xiao, A.M. Oliveira, L. Wang, Y. Zhao, T. Wang, J. Wang, B.P. Setzler, Y. Yan, Water-fed hydroxide exchange membrane electrolyzer enabled by a fluoride-incorporated nickel-iron oxyhydroxide oxygen evolution electrode, *ACS Catal.* 11 (2020) 264–270.
- [52] N. Chen, S.Y. Paek, J.Y. Lee, J.H. Park, S.Y. Lee, Y.M. Lee, High-performance anion exchange membrane water electrolyzers with a current density of 7.68 A cm^{-2} and a durability of 1000 h, *Energ. Environ. Sci.* 14 (2021) 6338–6348.
- [53] I. Vincent, E.C. Lee, H.M. Kim, Highly cost-effective platinum-free anion exchange membrane electrolysis for large scale energy storage and hydrogen production, *RSC Adv.* 10 (2020) 37429–37438.
- [54] D. Xu, M.B. Stevens, M.R. Cosby, S.Z. Oener, A.M. Smith, L.J. Enman, K.E. Ayers, C. B. Capuano, J.N. Renner, N. Danilovic, Y. Li, H. Wang, Q. Zhang, S.W. Boettcher, Earth-abundant oxygen electrocatalysts for alkaline anion-exchange-membrane water electrolysis: effects of catalyst conductivity and comparison with performance in three-electrode cells, *ACS Catal.* 9 (2018) 7–15.
- [55] X. Chen, Q. Wang, Y. Cheng, H. Xing, J. Li, X. Zhu, L. Ma, Y. Li, D. Liu, S-doping triggers redox reactivities of both iron and lattice oxygen in FeOOH for low-cost and high-performance water oxidation, *Adv. Funct. Mater.* 32 (2022) 2112674.
- [56] Y. Wu, Y. Zhao, P. Zhai, C. Wang, J. Gao, L. Sun, J. Hou, Triggering lattice oxygen activation of single-atomic Mo sites anchored on Ni-Fe oxyhydroxides nanoarrays for electrochemical water oxidation, *Adv. Mater.* (2022), e2202523.
- [57] N. Zhang, Y. Chai, Lattice oxygen redox chemistry in solid-state electrocatalysts for water oxidation, *Energ. Environ. Sci.* 14 (2021) 4647–4671.
- [58] N. Zhang, X. Feng, D. Rao, X. Deng, L. Cai, B. Qiu, R. Long, Y. Xiong, Y. Lu, Y. Chai, Lattice oxygen activation enabled by high-valence metal sites for enhanced water oxidation, *Nat. Commun.* 11 (2020) 4066.
- [59] Y. Sun, J. Wu, Y. Xie, X. Wang, K. Ma, Z. Tian, Z. Zhang, Q. Liao, W. Zheng, Z. Kang, Y. Zhang, Dynamics of both active phase and catalysis pathway for spinel water-oxidation catalysts, *Adv. Funct. Mater.* 32 (2022) 2207116.